Table 1. Patient characteristics

Patient characteristics	n	%
Age (mean ± SD, years)	63.5 ± 9.2	
Sex		
Female	47	63.5
Male	27	36.5
Tumor size (geometric mean ± SD, cm)	4.5 ± 2.1	
Regional LN		
N0	33	44.6
N1	41	55.4
TNM Stage		
Ia	4	5.4
Ib	4	5.4
IIa	5	5.4
IIb	9	6.7
III	8	10.8
IV	44	59.4
Tumor differentiation		
Well and moderately	41	55.4
Poor	33	44.6
Treatment		
Surgical resection	44	59.5
Palliative surgery or Supportive treatment	30	40.5
Total bilirubin (mean ± SD, mg/dL)	2.3 ± 5.2	
Direct bilirubin (mean ± SD, mg/dL)	1.5 ± 4.5	
Glucose (mean ± SD, mg/dL)	99.2 ± 19.2	
Amilase (mean ± SD, IU/L)	95.8 ± 103.3	
CA 19-9 (geometric mean ± SD, U/mL)	162.5 ± 5.75.8	
CEA (geometric mean ± SD, ng/mL)	2.3 ± 50.5	

has the potential to improve symptoms, quality of life, and survival (2). However, indications for surgical treatment and adjuvant chemotherapy should be evaluated carefully because of the high risk of procedure-related complications and side-effects. Therefore, prognostic factors permitting identification of those patients who will benefit from such treatment would be clinically useful (3).

18F-fluoro-2-deoxy-D-glucose (FDG) positron emission tomography (PET) is a useful modality that can assist in the diagnosis of pancreatic cancer, preoperative staging, evaluation of treatment response, and detection of recurrence (4). However, the prognostic value of FDG-PET scan in pancreatic cancer remains controversial. Several authors reported that increased value of standardized uptake of FDG at 1 hour after injection (SUV I) was associated with poor survival (5, 6). However, previous articles showed disagreement in the cut-off SUV that can distinguish patients with a good prognosis from those with a poor prognosis. On the other hand, our previous study did not confirm the value of SUV I as an independent prognostic marker in pancreatic cancer patient. The current study was performed to clarify these disagreements and to evaluate relations between the factors suggested to be related to the FDG accumulation in tumor tissue, such as glucose transporter-1 (GLUT-1), hexokinase type-II (HK-II), proliferating cell nuclear antigen (PCNA), and survival of pancreatic cancer patients.

MATERIALS AND METHODS

Patients

A total of 74 consecutive patients with pancreatic cancer were included in this study. Before enrolment in this study, each

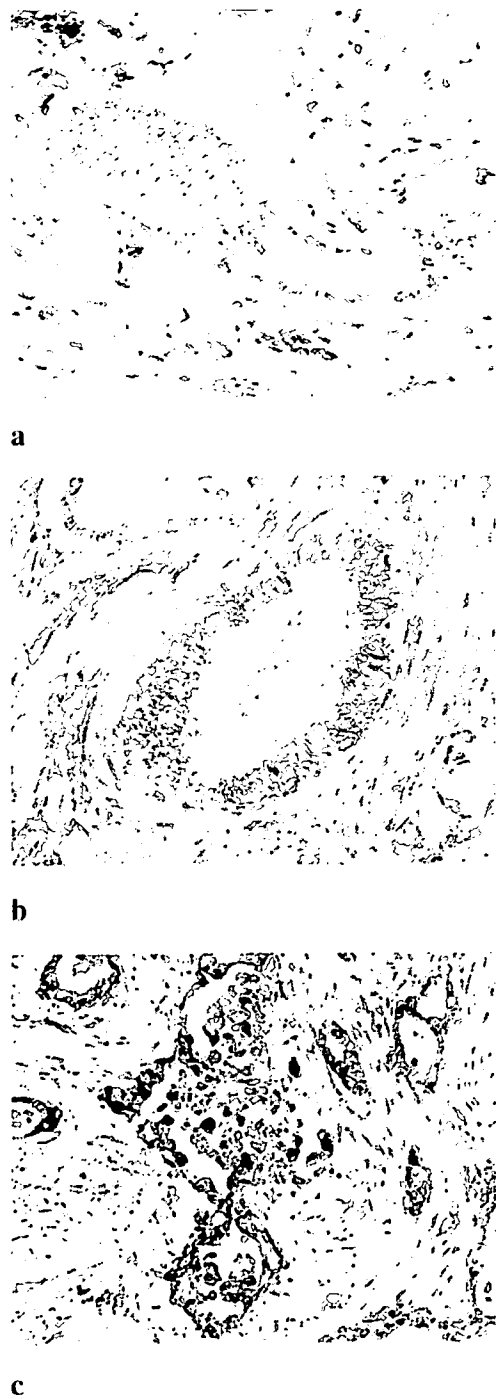

Figure 1. Typical examples of negative, moderate, strong GLUT-1 staining a) GLUT1 Index = 1 (0–20 percent); b) GLUT1 Index = 3 (40–60 percent); c). GLUT1 Index = 5 (80–100 percent).

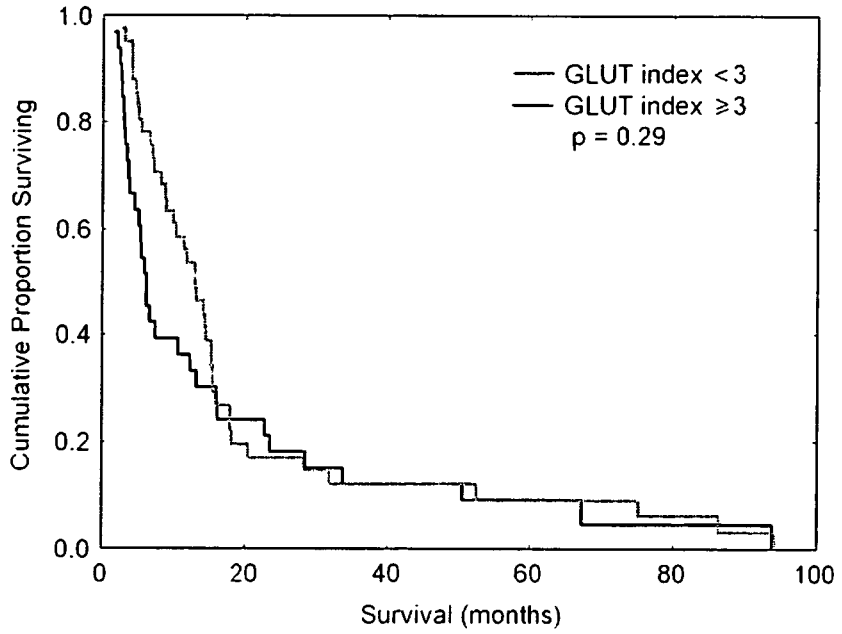

Figure 2. Cumulative survival for the patients with low (GLUT 1 index <3) (n = 41) and high (GLUT 1 index ≥3) (n = 33) expression of glucose transporter 1.

patient gave written informed consent, as required by the Kyoto University Human Study Committee. The mean age of the patients in our study was 63.5 ± 9.5 years (range, 40–81 years; 47 males and 27 females). Surgical resection of the tumor was performed in 44 patients (59.5 percent) and palliative surgery was performed in 30 patients (40.5 percent). Histopathological proof of pancreatic cancer was obtained in all cases. Cancer diagnosis and staging was based on the results of surgery and histopathological examination as well as on the results of physical examination. Computed tomography (CT), and other imaging modalities, such as magnetic resonance cholangiopancreatography (MRCP), endoscopic ultrasonography (EUS), and/or endoscopic retrograde cholangiopancreatography (ERCP). In addition, the following clinical data were recorded and analyzed for all patients: age and gender, tumor size, tumor differentiation, resectability, stage (AJCC/UICC TNM, 6th edition) (7), and patient's survival. Survival was determined from the date of the surgery to the last follow-up examination at Kyoto University Hospital or patient death. The main characteristics of the patients included in the study are summarized in Table 1.

Immunohistochemistry and histologic examination

Histological samples of pancreatic cancer tissue were obtained during surgical resection in 44 (59.5 percent), palliative surgery in 27 (36.5 percent) patients or core-needle biopsy during laparotomy in 3 (4.0 percent) patients. In all cases of core-needle biopsy, size of removed cancerous tissue sample was adequate for histological and immunohistochemical examination according to the selected study design.

Three or more paraffin sections per patient were processed for anti-GLUT-1, anti-HK-II, anti-PCNA immunostaining, and routine hematoxylin staining. The following anybodies were used: the polyclonal rabbit anti-human glucose transporter antibody (1:200, DAKO, Carpinteria, CA, USA), the polyclonal rabbit anti-rat hexokinase type II antibody (1:500, Chemicon International, Inc., Temecula, CA, USA), and the polyclonal mouse anti-rat proliferating cell nuclear antigen antibody (1:200, DAKO, Carpinteria, CA, USA).

Paraffin was removed from sections of each tumor using xylene and ethanol. Before immunohistochemical procedures, unmasking treatments were performed on all sections. Sections for anti-GLUT-1 immunostaining were incubated with Target Retrieval Solution (DAKO, Carpinteria, CA, USA), using the water bath method at 95–99°C for 60 minutes Sections for anti-HK-II and anti-PCNA immunostaining, were unmasked by the microwave method (strong range) using a distilled water bath for 15 minutes (5 minutes for each of 3 times).

After 20 minutes for cooling, the sections were washed with phosphate-buffered saline (PBS) (DAKO, Carpinteria, CA, USA) containing 20 mmol/L sodium phosphate and 150 mmol/L NaCl (pH 7.0), for 15 minutes (5 minutes for each of 3 times). Then, the endogenous peroxidase activity was blocked for 10 minutes at 25°C with 0.3 percent hydrogen peroxide in distilled water and the slides were washed with the PBS for 5 minutes. The nonspecific binding was blocked for 30 minutes at 25°C with blocking buffer (Blocker BLOTTO in TBS, Pierce, Rockford, IL, USA).

In the next step, each section was incubated with the anti-GLUT-1, anti-HK-II, or anti-PCNA antibody as a primary

antibody for 1 hour at 25°C. Then, all the sections were washed with PBS with 0.05 percent polyoxyethylene sorbitan monolaurate (Tween 20; Kanto Chemical Co., Tokyo, Japan) for 15 minutes. In the following steps, each section was stained by the horseradish peroxidase (HRP)-labeled polymer method, using an Envision Kit/HRP 3.3- diaminobenzidine tetrahydrochloride (DAB, DAKO, Carpinteria, CA, USA). For linking, the sections were incubated with the labeled polymer for 60 minutes at 25°C and washed with PBS with 0.05 percent Tween 20 for 15 minutes. As a substratechromogen solution, DAB was used at 25°C for 10 minutes diluted at 1 mg/mL with 0.05 mol/L Tris-HCl buffer, pH 7.5. All sections were then rinsed gently with distilled water and washed in flowing water for 5 minutes. In the final step, the sections were lightly counterstained with Mayer's hematoxylin and then dehydrated, and a coverslip was positioned with mounting medium. Other chemicals not mentioned were of the highest purity available. All slides were examined by light microscopy.

Immunohistochemical analysis for anti-GLUT-1, anti-HK-II, and anti-PCNA antibody was independently performed by 2 experienced physicians (T.H. and A.L.) who were blinded to the patient's survival. In each analysis, the percentages of strongly immunoreactive tumor cells in the total tumor cells were visually analyzed for each of 10 low-power fields (magnification. 10 × 10), and the averaged percentage was calculated and scored on a 5-point scale (1 = 0–20 percent, 2 = 20–40 percent, 3 = 40–60 percent, 4 = 60–80 percent, 5 = 80–100 percent) for each counting trial. Then, the 3 scores from all 3 counting trials were averaged again to give the GLUT-1 expression index (GLUT-1-index), HK-II expression index (HK-index), and PCNA expression index (PCNA-index). Although the expression of the GLUT-1 in pancreatic tumors was observed both in the cytoplasm and in the plasma membrane of the tumor cells, only expression of GLUT-1 transporter on the cell membrane was evaluated and scored in the present study.

Statistical analysis

The Kolmogorov-Smirnov test was used to check the normality of data distribution. Quantitative variables were compared using paired Student's t-test or Mann-Whitney test if their distribution were abnormal. Qualitative variables were compared using the chi-square test. Median survival curves were plotted using the Kaplan-Meier method. In univariate analysis, differences in survival were calculated with the log rank test. For quantitative variables, the different threshold levels were tested to find the one that could reveal the most significant difference in patient survival. In multivariate analysis, the associations between different varibales and overall survival were estimated using the Cox proportional hazard regression model. Quantitative data with normal distribution are presented as means ± SD; quantitative data with abnormal distribution are presented as geometric means ± SD, survival data are presented as median ± SD. Significance was defined as $p < 0.05$. Statistical analysis was performed by using a statistical software package StatView, version 5.0 (SAS Institute, Cary, NC, USA).

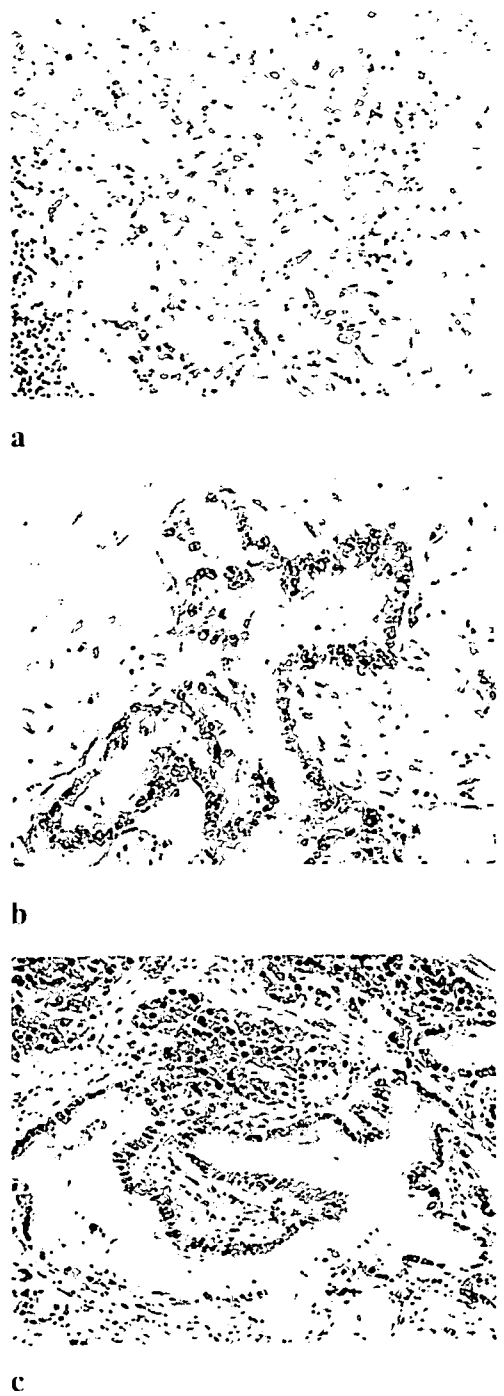

Figure 3. Typical examples, of negative, moderate, and strong HK-II staining a) HK-II Index = 1 (0–20 percent); b) HK-II Index = 3 (40–60 percent); c) HK-II Index = 5 (80–100 percent).

RESULTS

Patient characteristics

Overall median survival in the patients included in our study was 10.2 months (range, 1.6–94.5 months) with the 3-, 6-, 12- and 24- month survival being 89.2, 66.2, 45.9, and 17.6 percent, respectively.

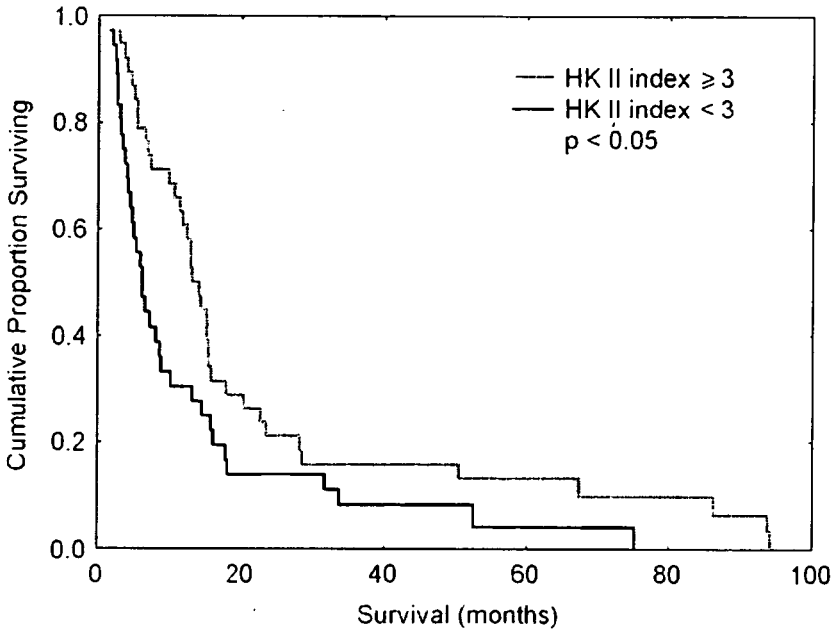

Figure 4. Cumulative survival for the patients with low (HK-II index <3) (n = 36) and high (HK-II index ≥3) (n = 38) expression of hexokinase type II.

Tumor characteristics

The mean size of the pancreatic tumors measured by histopathological examination of surgically resected specimens or measured on CT images in unresectable cases was 4.6 ± 2.0 cm (range, 1.0–11 cm). Patients with tumors <3 cm survived longer than those with larger lesions (15.3 versus 7.2 months, $p < 0.01$).

Regional lymph node involvement was diagnosed in 41 patients (55.4 percent) and was shown to be strongly associated with shorter survival. Patients with regional lymph node involvement survived 6.0 months, while patients without regional lymph node involvement survived 14.1 months ($p < 0.01$). Similar findings were observed for presence of distant metastasis, diagnosed in 41 patients (55.4 percent), was strongly associated with short patient survival. The median survival time for patients without distant metastasis was 14.1 months, while in patients who had distant metastasis (TNM Stage IV) it was only 6.0 months ($p < 0.01$).

Histological examinations revealed the histological types of pancreatic cancer, as follows: Invasive ductal adenocarcinoma in 64 (86.5 percent) patients, tubular adenocarcinoma in 3 (4.1 percent) patient, intraductal papillary carcinoma in one (1.4 percent) patient, intraductal papillary mucinous adenocarcinoma in 4 (5.4 percent) patients, and mucinous cystadenocarcinoma in 2 (2.6 percent) patients. There was no statistically significant difference in the survival rates between patients with different histological types of pancreatic cancer included in the present study.

Well or moderate differentiation of the tumors also was associated with better prognosis (14.1 months), compared with that of the patients with poorly differentiated pancreatic cancer (6.1 months, $p < 0.01$). Resectability of the tumor was associated with better survival. In 44 patients (59.5 percent) who underwent surgical resection, the median survival was 14.5 months, while in patients who received palliative surgery or supportive treatment only, it was 5.7 months ($p < 0.01$)

GLUT-1

GLUT-1 expression in pancreatic tumors occured both in the cytoplasm and in the plasma membrane of the tumor cells. The most intensive staining was observed on the membranes of the cancer cells, but GLUT-1 positive granules also were present through cytoplasm. Typical examples of strong, moderate, and negative GLUT-1 stainings are presented in Figure 1. The strong anti-GLUT-1 staining in red blood cells was used as a positive internal control. In the examined patients, pancreatic cancer cells showed different expression of GLUT-1 ranged from negative (GLUT-1 index = 1) in 29 patients (39.2 percent) to strongly positive (GLUT-1 index = 5) in 13 patients (17.6). The mean value of GLUT-1 index was 2.5 ± 1.5.

Our results did not show any significant correlation between GLUT-1 expression and patient's survival. None of the tested cut-off values of GLUT-1 indexes was able to separate patients in groups with different survival. Although we observed shorter survival in patients with high expression of GLUT-1 (GLUT-1 index ≥ 3) than in those with low expression of GLUT-1 (GLUT-1 index <3), this difference was not statistically significant (6.8 ± 22.1 versus 12.0 ± 21.4 months, respectively, $p = 0.29$) (Figure 2).

Hexokinase-II

Hexokinase type II expression occurred mainly in the cytoplasm of the tumor cells. Typical examples of strong, moderate and negative hexokinase type II staining are presented on the Figure 3. As well as GLUT-1 staining, pancreatic cancer cells showed different expression of HK-II ranged from negative (HK-II index = 1) in 24 patients (32.4 percent) to strongly positive (HK-II index = 5) in 21 patients (28.4 percent). The mean value of HK-II index was 2.9 ± 1.4.

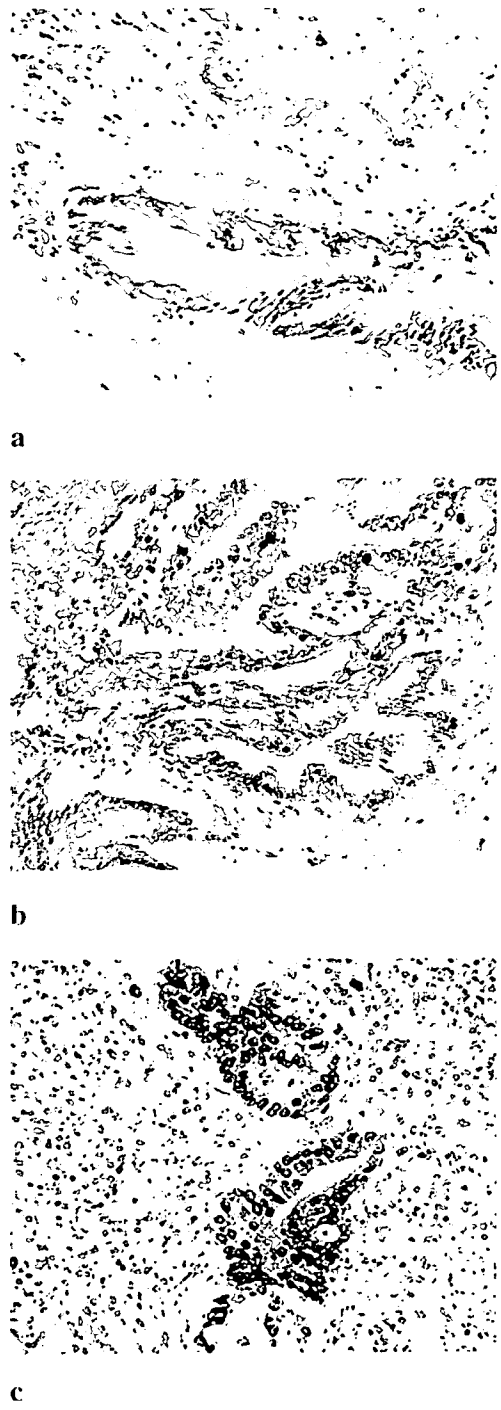

Figure 5. Typical examples of negative, moderate, and strong PCNA staining a) PCNA Index = 1 (0–20 percent); b) PCNA Index = 3 (40–60 percent); c. PCNA Index = 5 (80–100 percent).

In contrast with GLUT-1, expression of HK-II showed significant correlation with patient's survival. Out of the tested cut-off values of HK-II indexes, the cut of value of HK-II index = 3 could separate patients in groups with different survival: patients with high expression of HK-II (HK-II index ≥ 3) survived longer than those with low expression of HK-II (HK-II index <3) (13.5 ± 25.3 versus 6.1 ± 15.6 months, respectively, $p < 0.05$) (Figure 4).

PCNA

Proliferating cell nuclear antigen expression occurred in the nuclei of the tumor cells. Typical examples of strong, moderate and negative PCNA staining are presented on the Figure 5. As well as the other examined markers, pancreatic cancer cells showed different expression of PCNA ranged from negative (PCNA index = 1) in 24 patients (32.4 percent) to strongly positive (PCNA index = 5) in 11 patients (14.9 percent). The mean value of PCNA index was 2.4 ± 1.9.

In this study, level of PCNA expression showed the strongest correlation with patient's survival. Our of the tested cut-off values of PCNA indexes, the cut of value of PCNA index = 3 and PCNA index = 4 could separate patients in groups with different survival. However, the cut-off value of PCNA index = 4 yielded more statistically significant results. In the examined group of patients with high expression of PCNA (PCNA index ≥ 4) survived shorter than those with low expression of PCNA (PCNA index <4) (5.2 ± 4.0 versus 13.6 ± 23.7 months, respectively, $p < 0.01$) (Figure 6).

Multivariate analysis

When expression of HK-II and PCNA was combined (Figure 7), the patients with high expression of the HK-II and low expression of the PCNA (n = 28) showed the longest overall survival (15.3 ± 27.5 months). On the other hand, patients with low expression of the HK-II and high expression of the PCNA (n = 8) showed the shortest survival in the examined patients (4.4 ± 3.6 months, $p < 0.01$). Patients with low levels of HK-II and PCNA (n = 28), as well as the patients with high levels of HK-II and PCNA (n = 10) showed moderate survival (6.8 ± 17.2 and 6.1 ± 4.2, respectively, $p = 0.24$).

All factors showed prognostic significance in the univariate analysis were included in the multivariate model (Table 2). These variables were tumor size, regional lymph node involvement and distant metastasies, tumor respectability, and differentiation, as well as the HK-II and PCNA indexes. Out of them, only 2 factors showed an independent association with shorter patient survival: presence of distant metastsies (Beta Coefficient −0.88, standard error 0.31, t-value −2.83, $p < 0.01$), and PCNA-index ≥ 4 (Beta Coefficient −1.27, standard error 0.32, t-value −3.96, $p < 0.01$). Whole multivariate regression model was conceder adequate with chi-Square (Null model—final solution): 48.17 and $p < 0.001$.

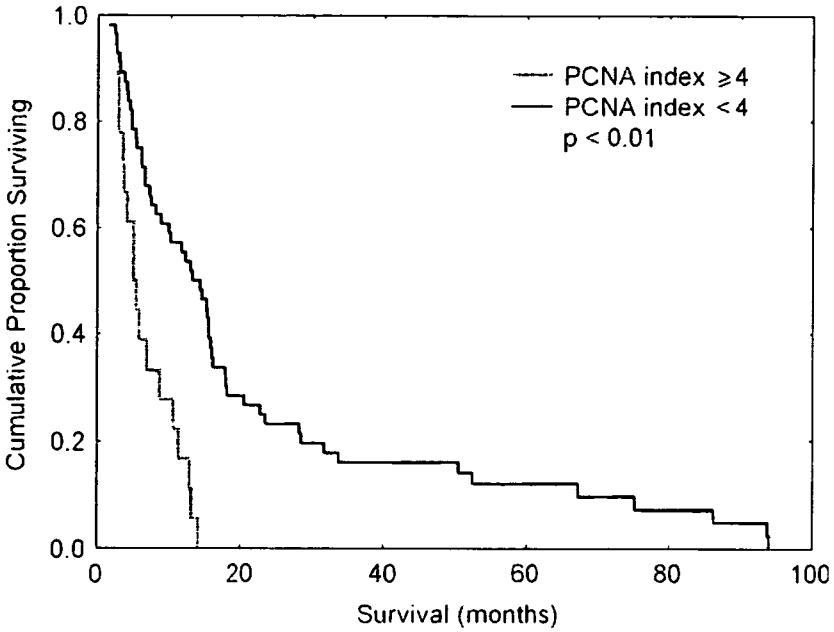

Figure 6. Cumulative survival for the patients with low (PCNA index <4) (n = 56) and high (PCNA index ≥ 4) (n = 18) expression of proliferation cell nuclear antigen.

DISCUSSION

In general, patients with pancreatic cancer have a very poor prognosis. Fewer than 1 percent survive more than 5 years from diagnosis (8). With such a background, it seems clinically important to identify subgroups of patints who may or may not benefit from aggressive therapy given in an attempt to improve survival (9). A variety of clinical and pathological factors have been reported to be associated with favorable prognosis in patients with pancreatic cancer, such as young age, small tumor size, tumor location in the head/body of the pancreas, surgical resection with negative resection margins, negative lymph node status, well/moderate tumor differentiation, diploid tumor DNA content, low serum levels of tumor markers (CA242, CA19-9,

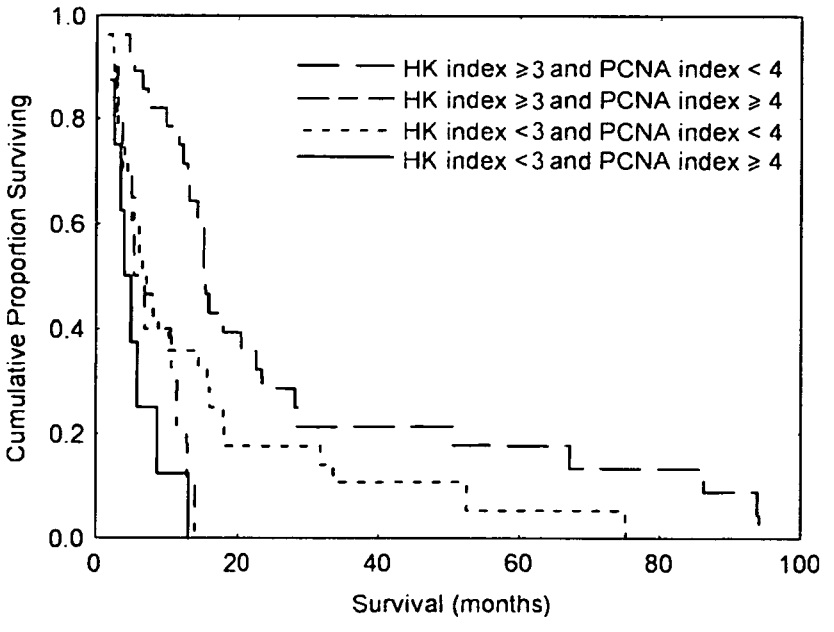

Figure 7. Cumulative survival for patients with high expression of the HK-II and low expression of the PCNA (n = 28); low expression of the HK-II, and high expression of the PCNA (n = 8): low levels of HK-II and PCNA (n = 28) and high levels of HK-II and PCNA (n = 10).

Table 2. Median survival in patients with pancreatic cancer

Prognostic factor	n	Survival (months ± SD)	P value univariate	P value multivariate
Tumor size				
<3 cm	16	15.3 ± 27.1	p < 0.01	n.s.
≥3 cm	58	7.2 ± 18.6		
Regional LN				
N0	33	14.1 ± 28.1	p < 0.01	n.s.
N1	41	6.0 ± 9.6		
Distant metastasis				
Absent	33	14.1 ± 28.1	p < 0.01	p < 0.05
Present	41	6.0 ± 9.6		
Tumor differentiation				
Well and moderately	41	14.1 ± 26.2	p < 0.01	n.s.
Poor	33	6.1 ± 10.1		
Treatment				
Surgical resection	44	14.5 ± 25.7	p < 0.01	n.s.
Palliative surgery or Supportive treatment	30	5.7 ± 5.2		
GLUT 1 index				
<3	41	12.0 ± 21.4	n.s.	—
≥3	33	6.8 ± 22.1		
HK II index				
<3	36	6.1 ± 15.6	p < 0.05	n.s.
≥3	38	13.5 ± 25.3		
PCNA index				
<4	56	13.6 ± 23.7	p < 0.01	p < 0.01
≥4	18	5.2 ± 4.0		

and MUC-1), and treatment with adjuvant chemoradiation (10). However, there is still controversy over factors, which can be used as independent predictors of prognosis and the significance of their influence on patient survival.

Prognostic value of the SUV of FDG at 1 hour after injection recently has been reported in breast, head and neck, and lung cancers, suggesting that tumor SUV is associated with poor survival (11, 12). Prognostic value of standardized uptake of FDG at 1 hour after injection in pancreatic cancer also has been reported by several authors (5, 6, 13, 14). However, there is disagreement over the prognostic significance of this method and over the cut-off SUV that can distinguish patients with a good prognosis from those with a poor prognosis. In contrast to these reportes, our previous results in the same group of patients, examined in the current study, did not show any prognostic value of early FDGPET in pancreatic cancer patients (15). On the other hand, dynamic assessment of FDG accumulation with dull-phase FDG-PET was shown to be a strong independent prognostic parameter.

GLUT-1 is one of the 8 structurally related membrane-bound facilitative glucose transporter proteins that have been studied extensively and well characterized (16). In many tumors, GLUT-1 expression is increased relative to corresponding normal tissue, and its overexpression correlates well with tumor hypoxia and poor prognosis in colorectal (17), non-small cell lung (18), and cervix carcinomas (19). Some other studies showed that GLUT-1 expression is related to FDG uptake and, therefore, can be evaluated with FDG-PET (20, 21). However, in contrast to other studies, our results did not show any significant correlation of GLUT-1 expression with the patient survival. Although we observed shorter survival in patients with high expression of GLUT-1, this tendency was not statistically significant.

Another key mediator of glycolysis and FDG-uptake in malignant cells is hexokinase type II that phosphorylates the sugar to hexose-6-phosphate. Under normal conditions, HK-II is the predominant hexokinase expressed in insulinsensitive tissues, and insulin regulates glucose metabolism and the expression of the isoenzyme. The levels of HK-II in cancer cells are regulated by similar factors that regulate GLUT-1 expression, for example transformation, carcinogenesis, hypoxia, and stress. Therefore, it was hypothesized that high HK-II expression might correlate with a worse patients prognosis (22). On the contrary, our data showed that the patients with high expression of hexokinase type II survived longer than those with low expression of hexokinase type II. According to the previous report by Higashi et al. (23), level of HK-II expression in the patients with pancreatic cancer can be predicted by Retention Index of FDG uptake, obtained from dual-phase FDG PET examination. Thus, dynamic, rather than static FDG-PET examination might estimate prognosis of pancreatic cancer patients.

PCNA is an intranuclear protein whose rate of the synthesis is at its maximum during the S-phase of the cell cycle. It functions as a cofactor for DNA polymerase, and is relate to DNA damage-repair mechanisms and cell proliferation (24). Nuclear immunoreactivity of PCNA also was found in the proliferative compartment of normal adult tissues, and was used as an index of cell proliferation in various tumors (25). Since PCNA is considered as a marker of proliferation, it is supposed to correlate with tumor aggressiveness, vascular invasion, and aggressive clinical behavior (26). Numerous studies demonstrated a negative prognostic impact of PCNA expression in patients with various neoplasms (27, 28).

Our results revealed that patients with high expression of PCNA survived shorter than those with low expression of PCNA. In addition, results of multivariate analysis (Table 2) showed that out of numerous prognostic criteria analyzed, only 2 factors showed an independent association with shorter patient survival: presence of distant metastsies, and PCNA-index ≥4. Unfortunately, at the current stage, there is only a limited data available on the correlation between the levels of PCNA expression and FDG uptake. Some reports showed a close correlation between FDG uptake and PCNA in head and neck and non-small cell lung cancer (29, 30). However, there has been no study reporting these the relationships in the pancreatic cancer. Therefore, future studies are required to evaluate the correlation between FDG uptake and PCNA in pancreatic cancer tissues.

CONCLUSION

Our results showed that in patients with pancreatic cancer, expression of glucose transporter 1 had no prognostic value. On the other hand, high levels of HK-II and low levels of PCNA expression, allow accurate identification of the patient with better prognosis and longer survival who may benefit from intensive anticancer treatment.

REFERENCES

1. Sarmiento, J.M.; Sarr, M.G. Staging strategies for pancreatic adenocarcinoma: what the surgeon really wants to know. Curr. Gastroenterol. Rep. **2003**, *5* 17–24.
2. Yeo, C.J.; Cameron J.L. Prognostic factors in ductal pancreatic cancer. Langenbecks Arch. Surg. **1998**, *393*, 129–133.
3. Lillemoe, K.D., Pitt, H.A. Palliation. surgical and otherwise. Cancer **1996**, *78*, 605–614.
4. Nakamoto, Y.; Higashi, T.; Sakahara, H; Tamaki, N,; Kogire, M.; et al. Delayed (18)F-fluoro-2-deoxy-D-glucose positron emission tomography scan for differentiation between malignant and benign lesions in the pancreas. Cancer **2000**, *89*, 2547–2554.
5. Nakata, B; Nishimura, S.; Ishikawa, T.; Ohira, M.; Nishino, H.; et al. Prognostic predictive value of 18F-fluorodeoxyglucose positron emission tomography for patients with pancreatic cancer. Int. J. Oncol. **2001**, *19*, 53–58.
6. Zimny, M.; Fass, J.; Bares, R.; Cremerius, U.; Sabri, O., et al. Fluorodeoxyglucose positron emission tomography and the prognosis of pancreatic carcinoma, Scand. J. Gastroenterol. **2000**, *35*, 883–888.
7. UICC, TNM Classification of Malignant Tumors, 6th edition. Sobin, L.H., Wittekind, Ch., eds., Wiley-Liss, New York. 2002.
8. Bramhall, S.R.; Allum, W.H.; Jones, A.G.; Allwood, A.; Cummins, C.; Neoptolemos, J.P. Treatment and survival in 13,560 patients with pancreatic cancer, and incidence of the disease, in the West Midlands: an epidemiological study. Br. J. Surg. **1995**, *82*, 111–115.
9. Ghaneh, P.: Kawesha, A.; Evans, J.D.; Neoptolemos, J.P. Molecular prognostic markers in pancreatic cancer. J. Hepatobiliary Pancreat. Surg. **2002**, 9–11.
10. Lim, J.E.; Chien, M.W.; Earle, C.C. Prognostic factors following curative resection for pancreatic adenocarcinoma. A population-based, linked databased analysis of 396 patients. Ann. Surg. **2003**, *237*, 74–85.
11. Buck, A. Schirrmeister, H., Kuhn, T.; Shen, C.; Kalker, T.; et al. FDG uptake in breast cancer: correlation with biological and clinical prognostic parameters. Eur. J. Nucl. Med. Mol. Imaging **2002**, *29*, 1317–1323.
12. Halfpenny, W.; Hain, S.F.; Biassoni, L.; Maisey, M.N.; Sherman, J.A.; McGurk, M. FDG-PET. A possible prognostic factor in head and neck cancer. Br. J. Cancer **2002**, *86*, 512–516.
13. Zimny, M.; Fass, J.; Bares, R.; Cremerius, U.; Sabri, O. et al. Fluorodeoxyglucose positron emission tomography and the prognosis of pancreatic carcinoma. Scand. J. Gastroenterol. **2003**, *35*, 883–8883.
14. Sperti, C.; Pasquali, C.; Chierichetti, F.; Ferronato, A.; Decet, G; Pedrazzoli, S. 18-Fluorodeoxyglucose positron emission tomography in predicting survival of patients with pancreatic carcinoma. J. Gastrointest. Surg. **2003**, *7*, 953–960.
15. Lyshchik, A.; Higashi, T.; Nakamoto, Y.; Fujimoto, K.; Doi, R.; Imamura, M.; Saga, T. Dual-phase (18)F-fluoro-2-deoxy-D: -glucose positron emission tomography as a prognostic parameter in patients with pancreaticcancer. Eur. J. Nucl. Med. Mol. Imaging **2005**, *32*, 389–397.
16. Burant, C.F.; Sivitz, W.I.; Fukumoto, H.; Kayano, T.; Nagamatsu, S.; et al. Mammalian glucose transporters; structure and molecular regulation. Recent Prog. Horm. Res. **1991**, *47*, 349–388.
17. Haber, R.S.; Rathan, A.; Weiser, K.R.; Pritsker, A.; Itzkowitz, S.H.; et al. Glut1 glucose transporter expression in colorectal carcinoma, Cancer **1998**, *83*, 34–40.
18. Younes, M.; Brown, R.W.; Stephenson, M.; Gondo, M.; Cagle, P.T. Overexpression of Glut1 and Glut3 in state 1 non-small cell lung carcinoma is associated with poor survival. Cancer **1997**, *80*, 1046–1051.
19. Airley, R.; Loncaster, J.; Davidson, S.; Bromley, M.; Roberts, S.; et al. Glucose transporter glut-1 expression correlates with tumor hypoxia and predicts metastasis-free survival in advanced carcinoma of the cervix. Clin. Cancer Res. **2001**, *7*, 928–934.
20. Higashi, T.; Tamaki, N.; Honda, T.; Torizuka, T.; Kimura, T.; et al. Expression of glucose transporters in human pancreatic tumors compared with increased FDG accumulation in PET study. J. Nucl. Med. **1997**, *38*, 1337–1344.
21. Higashi, T.; Tamaki, N.; Torizuka, T.; Nakamoto, Y.; Sakahara, H.; et al. FDG uptake, GLUT-1 glucose transporter and cellularity in human pancreatic tumors. J. Med. **1998**, *39*, 1727–1735.
22. Smith, T.A. FDG uptake, tumor characteristics and response to therapy: a review. Nucl. Med. Commun. **1998**. *19*, 97–105.
23. Higashi, T.; Saga, T.; Nakamoto, Y.; Ishimori, T.; Mamede, M.H.; et al. Relationship between retention index in dual-phase (18)F-FDG PET, and hexokinase-II and glucose transporter-1 expression in pancreatic cancer. J. Nucl. Med. **2002**, *43*, 173–80.
24. Bravo, R.; Rainer, F.; Blundell, P.A.; Macdonald-Bravo, H. Cyclin/PCNA is the auxiliary protein of DNA polymerase. Nature **1987**, *326*, 515–517.
25. Theunissen, P.H.; Leers, M.P.; Bollen, E.C. PCNA expression in formalin-fixed tissue of NSCLC. Histopathology **1992**, *20*, 251–255.
26. Oyama, T.; Mitsudomi, T.; Mizoue, T.; Ohgami, A.; Osaki, T.; Nakanishi, R.; Yasumoto, K. Proliferating cell nuclear antigen may be superior to argyrophilic nucleolar organizer region in predicting shortened survival of patients with non-small cell lung cancer. Surg. Oncol. **1995**, 83–89.
27. Fuji, M.; Motoi, M.; Saeki, H.; et al. Prognostic significance of proliferating cell nuclear antigen (PCNA) expresion in nonsmall cell lung cancer. Acta Med. Okayama **1993**, *47*, 103–103.
28. Esposito, V.; Baldi, A.; De Lucca, A.; et al. Prognostic value of p53 in non-small cell lung cancer: relationship with proliferating cell nuclear antigen and cigarette smoking. Hum. Pathol. **1997**, *28*, 233–237.
29. Jacob, R.; Welkoborsky, H.J.; Mann, W.J.; Jauch, M.; Amedee, R. [Fluorine-[8]fluorodeoxyglucose positron emission tomography. DNA ploidy and growth fraction in squamous-cell carcinomas of the head and neck. ORL J. Otorhinolaryngol. Relat. Spec. **2001**, *63*, 307–313.
30. Higashi, K.; Ueda, Y.; Yagishita, M.; Arisaka, Y.; Sakurai, A.; et al. FDG PET measurement of the proliferative potential of non-small cell lung cancer. J. Nucl. Med. **2000**, *41*, 85–92.

[CANCER RESEARCH 62, 860–866, February 1, 2002]

Rapid Accumulation and Internalization of Radiolabeled Herceptin in an Inflammatory Breast Cancer Xenograft with Vasculogenic Mimicry Predicted by the Contrast-enhanced Dynamic MRI with the Macromolecular Contrast Agent G6-(1B4M-Gd)$_{256}$

Hisataka Kobayashi,[1] Kazuo Shirakawa, Satomi Kawamoto, Tsuneo Saga, Noriko Sato, Akira Hiraga, Ichiro Watanabe, Yuji Heike, Kaori Togashi, Junji Konishi, Martin W. Brechbiel, and Hiro Wakasugi

Hitachi Medical Co. Chaired Departments of Diagnostic and Interventional Imagiology [H. K., S. K., K. T.] and Nuclear Medicine and Diagnostic Imaging [T. S., N. S., A. H., J. K.], Kyoto 606-8507, Japan; Pharmacology Division, National Cancer Center Research Institute, Tokyo 104-0045, Japan [K. S., I. W., Y. H., H. W.]; and Radioimmune and Inorganic Chemistry Section, Radiation Oncology Branch, National Cancer Institute, NIH, Bethesda, Maryland 20892 [M. W. B.]

ABSTRACT

The rapid blood flow and perfusion of macromolecules in the inflammatory breast cancer xenograft (WIBC-9), which exhibits a "vasculogenic mimicry" type of angiogenesis without the participation of endothelial cells and expresses high levels of the HER-2/*neu* antigen, was evaluated in mice using 3D-micro-MR angiography using a novel macromolecular MR contrast agent [G6-(1B4M-Gd)$_{256}$]. Herceptin, which recognizes the HER-2/*neu* antigen and has similar size (10 nm) to G6-(1B4M-Gd)$_{256}$, accumulated and internalized in the WIBC-9 tumors more quickly than in the control MC-5 tumors that progress with normal angiogenesis. Three dimensional micro-MRI with the G6-(1B4M-Gd)$_{256}$ macromolecular MRI contrast agent distinguishes between the different types of angiogenesis and is predictive of the rapid accumulation and internalization of Herceptin in the WIBC-9 inflammatory breast cancer xenograft.

INTRODUCTION

One of the major problems for antibody-mediated cancer therapy with radiolabeled antibodies and immunotoxins is their slow delivery from the circulation to the target cancer cells (1–3). This slow delivery is a source of toxic side effects to bone marrow, lung, and other organs (4–6). To enhance perfusion into cancerous tissue, chemically or genetically engineered small variants of antibodies have been evaluated with limited success (7–10). Therefore, intact antibodies are still being used in clinical cancer therapies (4, 6, 11–13).

Recently, several investigators have reported a new type of vasculogenesis called vasculogenic mimicry in IBC[2] osteosarcoma, and melanoma, wherein tumors can obtain nutrients by using alternative pathways without participation of endothelial cells (14–20). The vasculogenic mimicry was originally reported by Maniotis *et al.* (21) in aggressive melanoma that lacks evidence of significant necrosis and contains patterned networks of interconnected loops of extracellular matrix. The molecular basis for this vasculogenic mimicry in breast cancer has been reported (14, 22). The generation of microvascular channels by genetically deregulated, aggressive tumor cells was termed vasculogenic mimicry to emphasize their *de novo* generation of vascular channels without the participation of endothelial cells and the independence to angiogenesis. The significant blood flow in the vasculogenic mimicry has also been evaluated by the dynamic micro-MRI study (23). The presence of the endothelial cells, which retards the perfusion of macromolecular drugs into tumor tissue, has been one of the major problems in antibody-mediated therapies. In the current study, the syngenically xenografted tumor of IBC with vasculogenic mimicry was found to have significant flow between cancer cells without endothelial cells and to exhibit rapid perfusion of macromolecules as determined by the contrast-dynamic micro-MRI using G6-(1B4M-Gd)$_{256}$, a macromolecular MR contrast agent of similar molecular size to IgG, ~10 nm in diameter (24–29). Additionally, this vasculogenic mimicry with rapid perfusion was advantageous for the delivery of radiolabeled Herceptin, a Food and Drug Administration-approved humanized IgG against HER-2/*neu*, and permitted rapid access of the radioimmunoconjugate to the cancer cells.

MATERIALS AND METHODS

Herceptin. Herceptin, a humanized monoclonal antibody against the HER-2/*neu* antigen, was kindly provided by Dr. Thomas A. Waldmann, (Metabolism Branch, National Cancer Institute, NIH, Bethesda, MD).

Dendrimer. G6 (Aldrich Chemical Co., Milwaukee, WI) with an ethylenediamine core and 256 reactive exterior amino groups (M_r 57,991) was used for the preparation of the MRI contrast agent.

Establishment of WIBC-9 and MC-5. Tumor specimens from the patients with IBC and non-IBC were obtained immediately after surgery and processed as reported previously (30). The tumor xenografts were subsequently transplanted as described previously (14). This set of animal protocol experiments was approved by the Animal Use Committee of the National Cancer Center.

Conjugation of Chelates to Herceptin. Herceptin was concentrated to ~5 mg/ml and diafiltrated against 0.1 M PB at pH 9.0 with Centricon 50 (Amicon, Inc., Beverly, MA). The Herceptin was reacted with a 20-fold molar excess of 1B4M as described previously (31, 32).

Radiolabeling of Herceptin. Carrier-free $^{111}InCl_3$ was a gift from Japan Mediphysics (Nishinomiya, Japan), and ^{125}I was purchased from NEN DuPont (Boston, MA). Herceptin conjugated with 1B4M was reacted with ^{111}In in 0.3 M sodium acetate buffer at pH 6.0 for 15 min at room temperature as described previously (31).

Herceptin was labeled with ^{125}I by a modified chloramine-T method as described previously (32, 33). The specific activity of the radioiodinated antibody was 7 mCi/mg. Purity was >98% as determined by size-exclusion high-performance liquid chromatography using a TSK G2000SW column (TosoHaas, Philadelphia, PA; 0.1 M PBS; 0.01 M KCl; pH 7.4; 1 ml/min).

Immunoreactivity and Cell-binding Ability. The immunoreactivity of the radiolabeled Herceptin was determined using a cell-binding assay described previously (33). In brief, aliquots of ^{111}In-labeled or ^{125}I-labeled Herceptin (3 ng/100 μl) were incubated for 2 h at 4°C with ~1 × 10^7 WIBC-9 or MC-5 cells, which were obtained from the xenografted tumors. The cell-bound radioactivity was separated by centrifugation and counted in a gamma counter. Nonspecific binding to the cells was examined under conditions of antibody excess (50 μg of nonradiolabeled Herceptin). The specific binding was calculated as the percentage of binding subtracting the nonspecific binding.

Preparation of Macromolecular MR Contrast Agent for MR Angiography. The preparation of the G6-(1B4M-Gd)$_{256}$ macromolecular MR contrast agent (M_r 240,000) was described previously (25, 26). In brief, the G6

Received 7/12/01; accepted 11/30/01.

The costs of publication of this article were defrayed in part by the payment of page charges. This article must therefore be hereby marked *advertisement* in accordance with 18 U.S.C. Section 1734 solely to indicate this fact.

[1] To whom requests for reprints should be addressed, at Metabolism Branch, Building 10, Room 4N109, 10 Center Drive, National Cancer Institute, NIH, Bethesda, MD 20892. Phone: (301) 435-8344; Fax: (301) 496-9956; E-mail: hisataka@kuhp.kyoto-u.ac.jp.

[2] The abbreviations used are: IBC, inflammatory breast cancer; G6, generation-6 dendrimer; 1B4M, 2-(*p*-isothiocyanatobenzyl)-6-methyl-diethylenetriamine-pentaacetic acid.

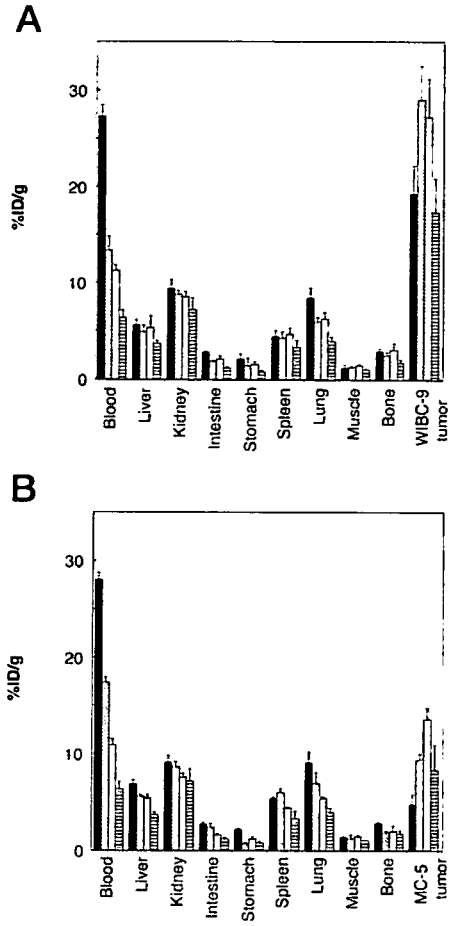

Fig. 1. Biodistribution of ^{111}In-labeled Herceptin in nude mouse xenografted with WIBC-9 (*A*) and MC-5 (*B*) tumors at 3 h (■), 1 day (▨), 2 days (□), and 4 days (▤) after injection. The data are expressed as the mean percentages of injected dose per gram of normal tissues and tumors; *bars*, ±SD (n = 4 or 5).

dendrimer was concentrated to ~5 mg/ml and diafilterated against a 0.1 M sodium phosphate buffer at pH 9.0 reacted with a 512-fold molar excess of 1B4M at 40°C and maintained at pH 9.0 with 1 M NaOH for 24 h. G6-1B4M$_{256}$ conjugate (~3 mg; containing 4 μmol 1B4M) was mixed with nonradioactive Gd(III) citrate (6 μmol) in 0.3 M ammonium citrate buffer for 2 h at 40°C. The excess Gd(III) was removed by diafiltration using the Centricon 30 (Amicon Co.) while simultaneously changing the buffer to 0.05 M PBS.

Biodistribution of Radiolabeled Herceptin in WIBC-9 Tumor-bearing Mice. Four groups of mice (n = 4–5) bearing either WIBC-9 or MC-5 tumor xenografts, were injected i.v. with both 2.5 μCi of ^{125}I-labeled Herceptin and 0.8 μCi of ^{111}In-labeled Herceptin. The mice were euthanized at 3 h, 1 d, 2 d, or 4 d after injection. Their blood was drawn and aliquoted for counting, and then their organs were harvested and counted in a gamma counter (Aloka, Mitaka, Japan). The data were expressed both as a percentage of injected dose per gram (%ID/g) of tissue and tumor:normal tissue ratios.

Dynamic Contrast Enhanced Micro-MRI of Tumor-bearing Mice with Macromolecular MR Contrast Agent. To evaluate the hemodynamics and perfusion of a macromolecule of similar size to Herceptin in these tumor models, dynamic micro-MRI of the tumor-bearing mice were obtained by injection of 0.03 mmolGd/kg of G6-(1B4M-Gd)$_{256}$ using a 1.5-Tesla superconductive magnet unit (Signa, General Electric Medical Systems, Milwaukee, WI), as described previously (34, 35). Six female 8-week-old BALB/c-*nu/nu* mice bearing WIBC-9 (n = 3) or MC-5 (n = 3) xenografts were used. For the dynamic study, the three-dimensional fast spoiled gradient echo technique [repetition time (TR)/echo time (TE) 10.5/2.7 msec; inversion time (TI) 31 msec; flip angle 30°; scan time 29 s; 1 number of excitation (NEX)] with chemical fat-suppression was used for all of the mice. The images were acquired at 30 s intervals at preinjection from 0 (immediately after injection) to 4.5 min after injection of the contrast agent. The coronal images were reconstructed with a 0.8-mm section thickness and with a 0.4-mm overlap. The field of view was 8 × 4 cm, and the size of matrix was 256 × 128. The delayed coronal MR images were obtained with the three-dimensional fast spoiled gradient echo technique (TR/TE 10.5/2.7; TI 31 ms; flip angle 30°; scan time 1 min 30 sec; 3NEX) with chemical fat-suppression used for all of the mice at 5 min postinjection immediately after the dynamic study. Additionally, the slice data were processed subtracting from postcontrast images to precontrast

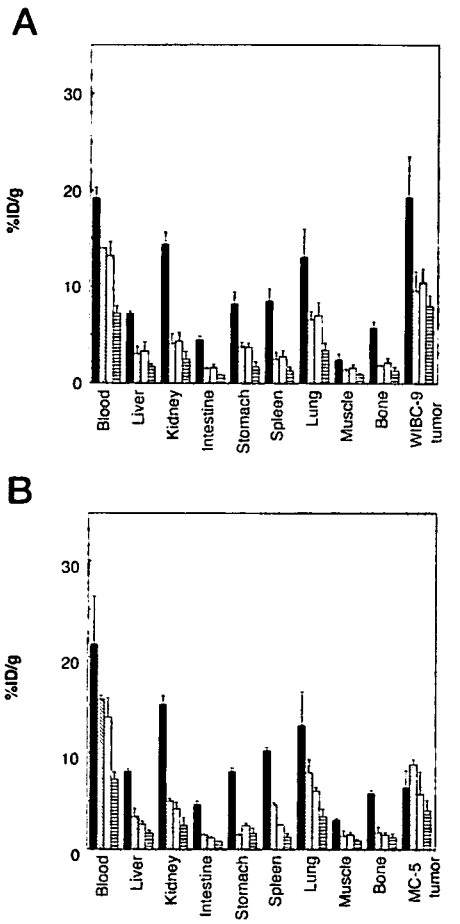

Fig. 2. Biodistribution of ^{125}I-labeled Herceptin in nude mouse xenografted with WIBC-9 (*A*) and MC-5 (*B*) tumors at 3 h (■), 1 day (▨), 2 days (□), and 4 days (▤) after injection. The data are expressed as the mean percentages of injected dose per gram of normal tissues and tumors; *bars*, ±SD (n = 4 or 5).

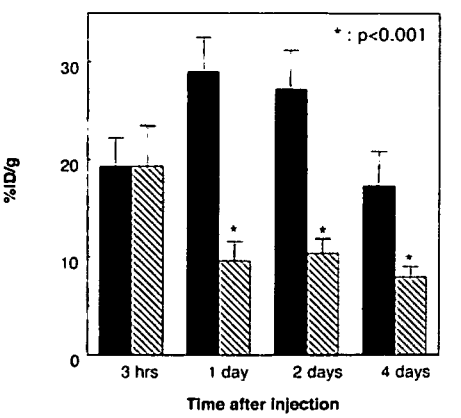

Fig. 3. Plots of the accumulation of ^{111}In-labeled and ^{125}I-labeled Herceptin in WIBC-9 tumor at 3 h (■), 1 day (▨), 2 days (□), and 4 days (▤) after injection. The data are expressed as the mean percentage of injected dose per gram of WIBC-9 tumor; *bars*, ±SD (n = 4 or 5). *, significant differences ($P < 0.01$).

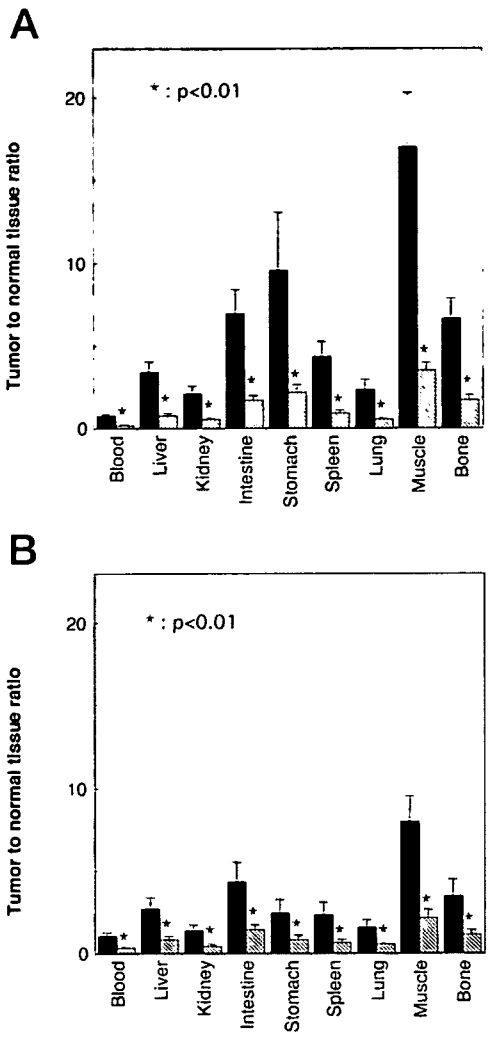

Fig. 4. Plots of serial WIBC-9 tumor:normal tissue ratio and MC-5 tumor:normal tissue ratio of ^{111}In-labeled Herceptin (*a*) and of ^{125}I-labeled Herceptin (*b*) in nude mice xenografted tumors at 3 h after injection. *, significant differences ($P < 0.01$).

images and constructed into three-dimensional MR angiograms using the maximum intensity projection method using the Advantage Windows (General Electric Medical Systems).

Scintigraphic Study. Scintigraphic imaging of the nude mice injected with ^{111}In-labeled Herceptin was performed; the mice, which were examined with dynamic micro-MRI using G6-(1B4M-Gd)$_{256}$, were injected i.v. with 100 μCi/28 μg of ^{111}In-labeled Herceptin. A gamma camera (Hitachi Medical Co., Tokyo, Japan) equipped with a 4-mm pin-hole collimator was used to perform scintigraphy at 3 h, 1 day, 2 days, and 4 days after injection. The mice were anesthetized with 1.15 mg of sodium pentobarbital (Dainabot, Osaka, Japan) per mouse. Imaging data were recorded in a 128-by-128 byte mode matrix using a 60% window centered over the 250 keV energy peak of ^{111}In. Images were acquired for 200,000 counts.

Histological Comparison with MRI and Scintigraphic Images. The mice were killed with an injection of 10 mg of sodium pentobarbital via the tail vein immediately after the final series of examinations and fixed in formaldehyde for >2 weeks. The tumors were sectioned in the same coronal planes as the MR sectional images, examined by stereoscopic microscopy (Photomakroskop; Wild, Heerbrugg, Switzerland), and correlated with the serial MR images. Additionally, the coronal histological sections of the tumors stained with H&E were correlated with the MR images. All of the studies reported herein were approved by the Animal Care Committee of Kyoto University.

Statistical Analysis. Statistical analysis was performed using Student's *t* test (StatView; SAS Institute Inc., Cary, NC).

RESULTS

Immunoreactivity and Cell-binding Ability. The maximum specific binding of the ^{111}In-labeled Herceptin to the WIBC-9 and the MC-5 cells was 82% and 18%, respectively. The maximum specific binding of the ^{125}I-labeled Herceptin to the WIBC-9 and the MC-5 cells was 78% and 16%, respectively. Ninety-five percent of their binding was inhibited by the addition of 50 μg of nonradiolabeled Herceptin.

Biodistribution of Radiolabeled Herceptin in WIBC-9 Tumor-bearing Mice. The biodistribution of radiolabeled Herceptin in the normal organs exhibited no significant differences at most time points between mice bearing either WIBC-9 or MC-5 tumors (Figs. 1 and 2). However, both ^{111}In- and ^{125}I-labeled Herceptin accumulated in the WIBC-9 tumors significantly higher than in the MC-5 tumors at 3 h after injection ($P < 0.01$). Although the ^{111}In-labeled Herceptin

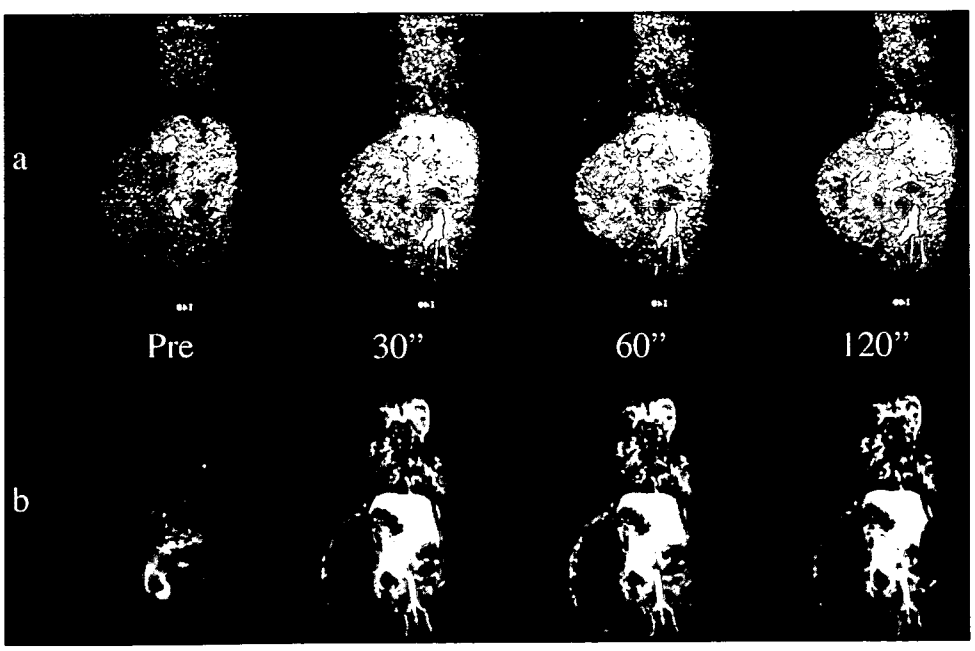

Fig. 5. Contrast-enhanced dynamic two-dimensional micro-MRI of a mouse bearing WIBC-9 (*a*) or MC-5 (*b*) tumors using 0.03 mmolGd/kg of G6-(1B4M-Gd)$_{256}$ macromolecular MR contrast agent at preinjection and 30, 60, and 120 s after injection of the contrast agent. Diffuse enhancement of the WIBC-9 tumor was shown at 30 min after injection. However, only the vascular structure was shown in the MC-5 tumor without diffuse enhancement of the tumor tissue up to 120 s after injection.

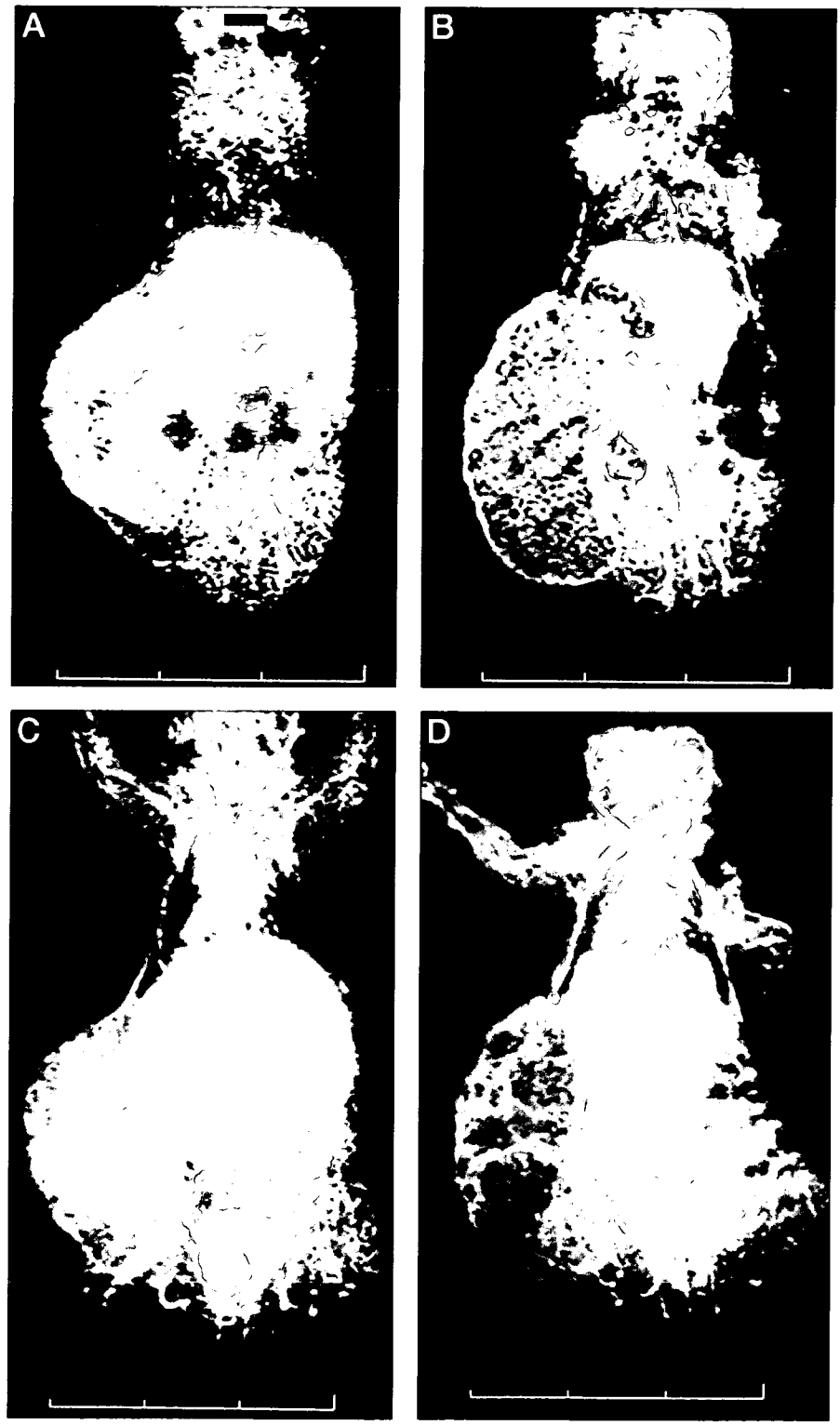

Fig. 6. Contrast-enhanced two-dimensional micro-MRI (*a* and *b;* sectional images) and three-dimensional micro-MR angiography (*c* and *d:* maximum intensity projection images) of a mouse bearing WIBC-9 (*a, c*) or MC-5 (*b, d*) tumors using 0.03 mmolGd/kg of G6-(1B4M-Gd)$_{256}$ macromolecular MR contrast agent at 5 min after injection of the contrast agent. Diffuse enhancement of the WIBC-9 tumor was shown. However, only the vascular structure was shown in the MC-5 tumor without diffuse enhancement of the tumor tissue.

accumulated in the WIBC-9 tumors significantly higher than in the MC-5 tumors up to 4 days after injection, the accumulation of ^{125}I-labeled Herceptin in the WIBC-9 tumor decreased at 1 day after injection and later was significantly lower than that of the ^{111}In-labeled Herceptin (Fig. 3). The tumor:normal tissue ratio in all of the organs was significantly higher in mice bearing WIBC-9 tumors than in mice bearing MC-5 tumors, especially at 3 h after injection (Fig. 4).

Dynamic Contrast Enhanced Micro-MRI of Tumor-bearing Mice with Macromolecular MR Contrast Agent. The serial dynamic MRI using the macromolecular contrast agent G6-(1B4M-Gd)$_{256}$ showed a more rapid and more diffuse enhancement of the WIBC-9 tumor than that of the MC-5 tumor (Fig. 5). Both two-dimensional micro-MRI (Fig. 6, *a* and *b*) and three-dimensional dynamic micro-MR angiography (Fig. 6, *c* and *d*) of tumor-bearing nude mice using the macromolecular contrast agent G6-(1B4M-Gd)$_{256}$, which had similar size to that of Herceptin, (24, 28, 29) showed significantly better diffusion and early contrast enhancement in the WIBC-9 tumor than in the MC-5 tumor as indicated by the micro-MR angiograms.

Scintigraphic Study. The scintigrams of tumor-bearing mice indicated high homogeneous accumulation of the ^{111}In-labeled Hercep-

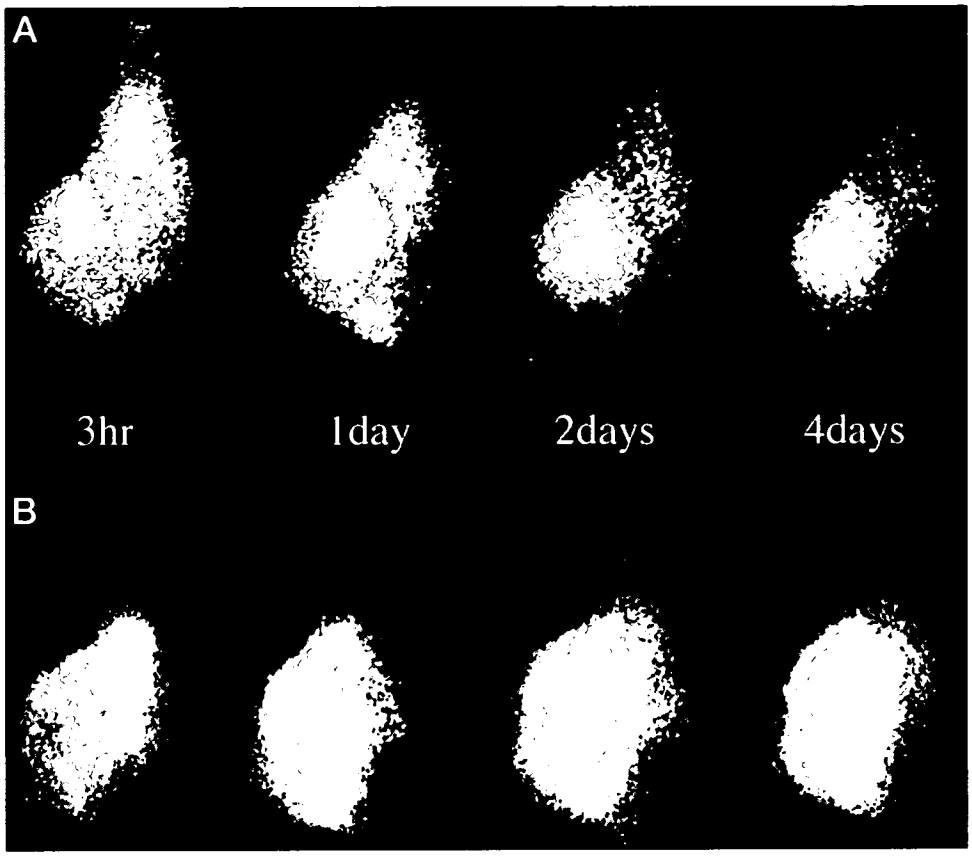

Fig. 7. A series of scintigrams of the same mouse bearing the WIBC-9 (*a*) or the MC-5 (*b*) tumor as shown in Figs. 5–7 were obtained at 3 h, 1, 2, and 4 days after injection. Higher and more homogeneous accumulation of ^{111}In-labeled Herceptin was shown in WIBC-9 tumor than MC-5 tumor, which showed no central accumulation, within 3 h after injection. The tumor-to-background contrast was better in longer time point after injection. In addition, the WIBC9 tumor-to-background contrast was better than the MC-5 tumor-to-background contrast, which is consistent with the biodistribution data shown in Figs. 1 and 2.

tin in the WIBC-9 tumors within 3 h after injection (Fig. 7) compared with that in the MC-5 tumor. The WIBC-9 tumor-to-background contrast improved at later time points after injection. These results were consistent with the biodistribution data shown in Figs. 1 and 2.

Histological Comparison with MRI and Scintigraphic Images. Numerous RBCs existing in the channel components, called vasculogenic mimicry, were shown to be present especially at the inner part of the WIBC-9 tumor (Fig. 8*a*). This correlates with the rapid, diffusion contrast enhancement on the dynamic MRI with G6-(1B4M-Gd)$_{256}$ macromolecular contrast agent (Fig. 6, *a* and *c*) and the quick accumulation of the ^{111}In-labeled Herceptin in the scintigraphic image obtained at 3 h after injection (Fig. 7*a*). However, this finding of vasculogenic mimicry was sometimes misread by pathologists as an artifact or subtle intratumoral hemorrhage. In contrast, the MC-5 tumor showed the central necrotic foci. In addition, the capillaries in the MC-5 tumor were lined with endothelial cells. This correlates with the absent contrast enhancement on the dynamic MRI with G6-(1B4M-Gd)$_{256}$ macromolecular contrast agent (Fig. 6, *b* and *d*) and the luck accumulation of the ^{111}In-labeled Herceptin in the scintigraphic image obtained at 3 h after injection (Fig. 7*b*).

DISCUSSION

HER-2 is a membrane receptor of which the overexpression is strongly associated with poor prognosis in breast cancers (36, 37). Inhibition of HER-2 activity can reduce or inhibit tumor growth, which led to the development of Herceptin, a Food and Drug Administration-approved recombinant humanized anti-HER-2 monoclonal antibody now in clinical use (38–40). However, the objective response rate to Herceptin monotherapy is actually quite low (41). Therefore, Herceptin armed with cytotoxic radionuclides of other cytotoxic agents to augment the biological activity and to capitalize on the selective delivery action is a promising therapeutic approach.

One of the major problems in the use of whole IgG for cancer therapy is slow perfusion into tumor tissue because of both size and competing catabolism. In regard to the perfusion of macromolecules like an IgG, vasculogenic mimicry-like angiogenesis, a condition in which the tumor vascular channels are not lined by endothelial cells, is advantageous. In the present study, radiolabeled Herceptin accumulated to the xenografted WIBC-9 tumors more rapidly and higher than to the MC-5 tumors, and a clear scintigraphic image could be obtained as early as 3 h after injection of ^{111}In-labeled Herceptin. The discrepancy between the accumulation of the ^{111}In-labeled and the ^{125}I-labeled antibody was reported to be a consequence of the internalization of the antibodies and subsequent dehalogenation (9, 42). The high accumulation of both ^{111}In-labeled and ^{125}I-labeled Herceptin at 3 h after injection and the discrepant accumulation between them at 1 day after injection provide evidence that the Herceptin quickly accumulated and was internalized into the WIBC-9 cells. Therefore, the WIBC-9, which is characterized as a tumor accompanied with the formation of vascular channels without endothelial cells, might be an optimal target for developing antibody-based therapies with radiometal-labeled or toxin-conjugated Herceptin rather than antibody-dependent cellular cytotoxicity induced by Herceptin itself because of this rapid internalization.

In addition, although scintigraphy with radiolabeled albumin or antibodies is the only available method to evaluate the perfusion of macromolecules, spatial resolution is quite limited. In this study, high-resolution micro-MRI with a macromolecular contrast agent, G6-(1B4M-Gd)$_{256}$, (25, 26) was used to evaluate the perfusion of the macromolecule. In the current study as well as in previous studies, three-dimensional micro-MRI of tumors with well-known types of

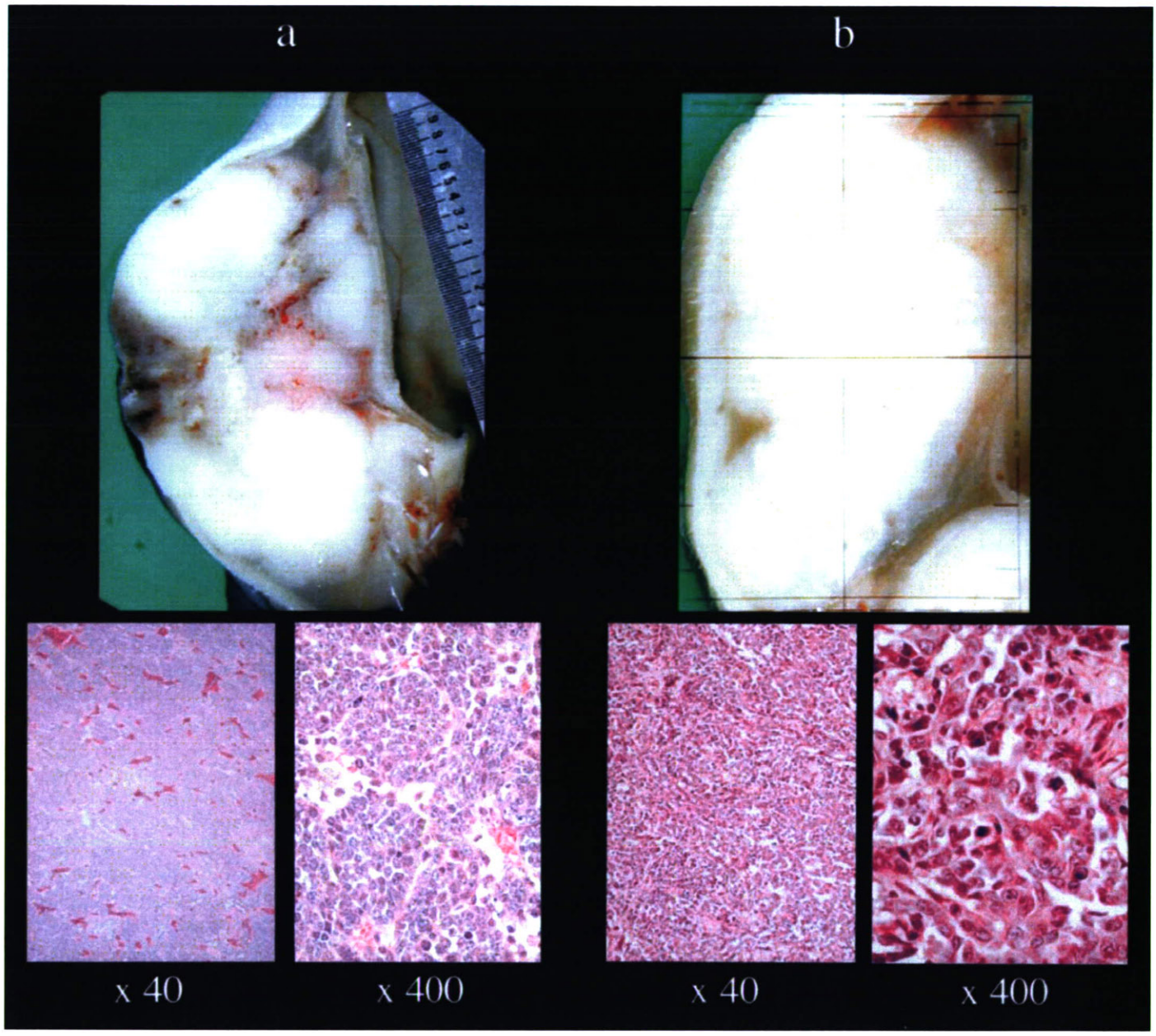

Fig. 8. Stereoscopic (×10) and light (×40 and ×400) microscopy pictures of WIBC-9 (*a*) or MC-5 (*b*) tumor. WIBC-9 showed the solid white tumor without necrotic foci and numerous small vascular channels without lining endothelial cells, which corresponded to vasculogenic mimicry. In contrast, MC-5 showed the white tumor with central necrotic foci. All capillaries in MC-5 tumors were lined by the endothelial cells.

vasculogenesis lined by endothelial cells such as those obtained from the MC-5 and LS180 cell lines depicted only continuous vascular structure and no diffuse enhancement in the tumors within 5 min after injection of G6-(1B4M-Gd)$_{256}$ (35). The diffuse enhancement in the tumor tissue was shown only in the WIBC-9 tumor by the three-dimensional micro-MRI within 5 min after injection. These diffuse enhancement areas as indicated by MR corresponded well to the areas where radiolabeled Herceptin accumulated. These findings in the WIBC-9 tumors are also compatible and indicative of the special type of angiogenesis termed vasculogenic mimicry, a type of vasculogenesis without the involvement of endothelial cells; thus no barrier exists for Herceptin to efficiently access these cancer cells (14).

In conclusion, contrast-enhanced dynamic micro-MRI with a G6-(1B4M-Gd)$_{256}$ macromolecular MR contrast agent was able to evaluate the intratumoral perfusion of macromolecules because of different types of angiogenesis and was predictive of the rapid accumulation and internalization of Herceptin in the IBC xenograft WIBC-9.

ACKNOWLEDGMENTS

We thank Dr. Thomas A. Waldmann of the Metabolism Branch, National Cancer Institute, NIH, for kindly providing the Herceptin for this study and for assistance in the preparation of this manuscript.

REFERENCES

1. Yokota, T., Milenic, D. E., Whitlow, M., and Schlom, J. Rapid tumor penetration of a single-chain Fv and comparison with other immunoglobulin forms. Cancer Res., *52:* 3402–3408, 1992.
2. Kobayashi, H., Sakahara, H., Hosono, M., Yao, Z. S., Toyama, S., Endo, K., and Konishi, J. Improved clearance of radiolabeled biotinylated monoclonal antibody following the infusion of avidin as a chase without decreased accumulation in the target tumor. J. Nucl. Med., *35:* 1677–1684, 1994.

3. Saga, T., Neumann, R. D., Heya, T., Sato, J., Kinuya, S., Le, N., Paik, C. H., and Weinstein, J. N. Targeting cancer micrometastases with monoclonal antibodies: a binding-site barrier. Proc. Natl. Acad. Sci. USA, *92:* 8999–9003, 1995.
4. Press, O. W., Eary, J. F., Appelbaum, F. R., Martin, P. J., Badger, C. C., Nelp, W. B., Glenn, S., Butchko, G., Fisher, D., Porter, B., Matthews, D. C., Fisher, L. D., and Bernstein, I. D. Radiolabeled-antibody therapy of B-cell lymphoma with autologous bone marrow support. N. Engl. J. Med., *329:* 1219–1224, 1993.
5. Pai, L. H., Wittes, R., Setser, A., Willingham, M. C., and Pastan, I. Treatment of advanced solid tumors with immunotoxin LMB-1: an antibody linked to *Pseudomonas* exotoxin. Nat. Med., *2:* 350–353, 1996.
6. Waldmann, T. A., White, J. D., Carrasquillo, J. A., Reynolds, J. C., Paik, C. H., Gansow, O. A., Brechbiel, M. W., Jaffe, E. S., Fleisher, T. A., Goldman, C. K., Top, L. E., Bamford, R., Zaknoen, S., Roessler, E., *et al.* Radioimmunotherapy of interleukin-2R α-expressing adult T-cell leukemia with yttrium-90-labeled anti-Tac. Blood, *86:* 4063–4075, 1995.
7. Kobayashi, H., Yoo, T. M., Kim, I. S., Kim, M-K., Le, N., Webber, K. O., Pastan, I., Paik, C. H., Eckelman, W. C., and Carrasquillo, J. A. L-lysine effectively blocks renal uptake of ^{125}I- or ^{99m}Tc-labeled anti-Tac dsFv. Cancer Res., *56:* 3788–3795, 1996.
8. Kreitman, R. J., Wilson, W. H., Robbins, D., Margulies, I., Stetler-Stevenson, M., Waldmann, T. A., and Pastan, I. Responses in refractory hairy cell leukemia to a recombinant immunotoxin. Blood, *94:* 3340–3348, 1999.
9. Kobayashi, H., Kao, C. H., Kreitman, R. J., Le, N., Kim, M. K., Brechbiel, M. W., Paik, C. H., Pastan, I., and Carrasquillo, J. A. Pharmacokinetics of 111In- and ^{125}I-labeled antiTac single-chain Fv recombinant immunotoxin. J. Nucl. Med., *41:* 755–762, 2000.
10. Kreitman, R. J., and Pastan, I. Accumulation of a recombinant immunotoxin in a tumor *in vivo*: fewer than 1000 molecules per cell are sufficient for complete responses. Cancer Res., *58:* 968–975, 1998.
11. Kaminski, M. S., Zasadny, K. R., Francis, I. R., Fenner, M. C., Ross, C. W., Milik, A. W., Estes, J., Tuck, M., Regan, D., Fisher, S., Glenn, S. D., and Wahl, R. L. Iodine-131-anti-B1 radioimmunotherapy for B-cell lymphoma. J. Clin. Oncol., *14:* 1974–1981, 1996.
12. Kaminski, M. S., Estes, J., Zasadny, K. R., Francis, I. R., Ross, C. W., Tuck, M., Regan, D., Fisher, S., Gutierrez, J., Kroll, S., Stagg, R., Tidmarsh, G., and Wahl, R. L. Radioimmunotherapy with iodine (131)I tositumomab for relapsed or refractory B-cell non-Hodgkin lymphoma: updated results and long-term follow-up of the University of Michigan experience. Blood, *96:* 1259–1266, 2000.
13. Behr, T. M., Sharkey, R. M., Juweid, M. E., Dunn, R. M., Vagg, R. C., Ying, Z., Zhang, C. H., Swayne, L. C., Vardi, Y., Siegel, J. A., and Goldenberg, D. M. Phase I/II clinical radioimmunotherapy with an iodine-131-labeled anti- carcinoembryonic antigen murine monoclonal antibody IgG. J. Nucl. Med., *38:* 858–870, 1997.
14. Shirakawa, K., Tsuda, H., Heike, Y., Kato, K., Asada, R., Inomata, M., Sasaki, H., Kasumi, F., Yoshimoto, M., Iwanaga, T., Konishi, F., Terada, M., and Wakasugi, H. Absence of endothelial cells, central necrosis, and fibrosis are associated with aggressive inflammatory breast cancer. Cancer Res., *61:* 445–451, 2001.
15. Folkman, J., and Klagsbrun, M. Angiogenic factors. Science (Wash. DC), *235:* 442–447, 1987.
16. Weidner, N., Semple, J. P., Welch, W. R., and Folkman, J. Tumor angiogenesis and metastasis: correlation in invasive breast carcinoma. N. Engl. J. Med., *324:* 1–8, 1991.
17. Kalka, C., Masuda, H., Takahashi, T., Kalka-Moll, W. M., Silver, M., Kearney, M., Li, T., Isner, J. M., and Asahara, T. Transplantation of *ex vivo* expanded endothelial progenitor cells for therapeutic neovascularization. Proc. Natl. Acad. Sci. USA, *97:* 3422–3427, 2000.
18. Isner, J. M., and Asahara, T. Angiogenesis and vasculogenesis as therapeutic strategies for postnatal neovascularization. J. Clin. Investig., *103:* 1231–1236, 1999.
19. Takahashi, T., Kalka, C., Masuda, H., Chen, D., Silver, M., Kearney, M., Magner, M., Isner, J. M., and Asahara, T. Ischemia- and cytokine-induced mobilization of bone marrow-derived endothelial progenitor cells for neovascularization. Nat. Med., *5:* 434–438, 1999.
20. Murohara, T., Ikeda, H., Duan, J., Shintani, S., Sasaki, K., Eguchi, H., Onitsuka, I., Matsui, K., and Imaizumi, T. Transplanted cord blood-derived endothelial precursor cells augment postnatal neovascularization. J. Clin. Investig., *105:* 1527–1536, 2000.
21. Maniotis, A. J., Folberg, R., Hess, A., Seftor, E. A., Gardner, L. M., Pe'er, J., Trent, J. M., Meltzer, P. S., and Hendrix, M. J. Vascular channel formation by human melanoma cells *in vivo* and *in vitro*: vasculogenic mimicry. Am. J. Pathol., *155:* 739–752, 1999.
22. Hendrix, M. J., Seftor, E. A., Kirschmann, D. A., and Seftor, R. E. Molecular biology of breast cancer metastasis. Molecular expression of vascular markers by aggressive breast cancer cells. Breast Cancer Res. Treat., *2:* 417–422, 2000.
23. Shirakawa, K., Kobayashi, H., Heike, Y., Kawamoto, S., Brechbiel, M. W., Kasumi, F., Iwanaga, T., Konishi, F., Terada, M., and Wakasugi, H. Hemodynamics in vasculogenic mimicry and angiogenesis of inflammatory breast cancer xenograft. Cancer Res.*62:* 560–566, 2002.
24. Tomalia, D. A., Naylor, A. M., and Goddard, W. A., III. Starburst dendrimers: molecular-level control of size, shape, surface chemistry, topology, and flexibility from atoms to macroscopic matter. Angew. Chem. Int. Ed. Engl., *29:* 138–175, 1990.
25. Kobayashi, H., Sato, N., Hiraga, A., Saga, T., Nakamoto, Y., Ueda, H., Konishi, J., Togashi, K., and Brechbiel, M. W. 3D-micro-MR angiography of mice using macromolecular MR contrast agents with polyamidoamine dendrimer core with references to their pharmacokinetic properties. Magn. Reson. Med., *45:* 454–460, 2001.
26. Kobayashi, H., Sato, N., Kawamoto, S., Saga, T., Hiraga, A., Haque, T. L., Ishimori, T., Konishi, J., Togashi, K., and Brechbiel, M. W. Comparison of the macromolecular MR contrast agents with ethylenediamine-core *versus* ammonia-core generation-6 polyamidoamine dendrimer. Bioconjug. Chem., *12:* 100–107, 2001.
27. Lascombe, M. B., Alzari, P. M., Boulot, G., Saludjian, P., Tougard, P., Berek, C., Haba, S., Rosen, E. M., Nisonoff, A., and Poljak, R. J. Three-dimensional structure of Fab R19.9, a monoclonal murine antibody specific for the p-azobenzenearsonate group. Proc. Natl. Acad. Sci. USA, *86:* 607–611, 1989.
28. Alzari, P. M., Lascombe, M. B., and Poljak, R. J. Three-dimensional structure of antibodies. Annu. Rev. Immunol., *6:* 555–580, 1988.
29. Guillon, V., Alzari, P. M., and Poljak, R. J. Preliminary crystallographic study of a complex between an heteroclitic anti-hen egg-white lysozyme antibody and the heterologous antigen pheasant egg-white lysozyme. J. Mol. Biol., *197:* 375–376, 1987.
30. Pezzella, F., Pastorino, U., Tagliabue, E., Andreola, S., Sozzi, G., Gasparini, G., Menard, S., Gatter, K. C., Harris, A. L., Fox, S., Buyse, M., Pilotti, S., Pierotti, M., and Rilke, F. Non-small-cell lung carcinoma tumor growth without morphological evidence of neo-angiogenesis. Am. J. Pathol., *151:* 1417–1423, 1997.
31. Wu, C., Brechbiel, M. W., Kozak, R. W., and Gansow, O. A. Metal-chelate-dendrimer-antibody constructs for use in radioimmunotherapy and imaging. Bioorg. Med. Chem. Lett., *4:* 449–454, 1994.
32. Kobayashi, H., Sakahara, H., Saga, T., Hosono, M., Shirato, M., Kanda, H., Ishibashi, K., Watanabe, T., Endo, K., Ishiwata, I., and Konishi, J. A human/mouse chimeric monoclonal antibody against CA125 for radioimmunoimaging of ovarian cancer. Cancer Immunol. Immunother., *37:* 143–149, 1993.
33. Kobayashi, H., Wu, C., Kim, M. K., Paik, C. H., Carrasquillo, J. A., and Brechbiel, M. W. Evaluation of the *in vivo* biodistribution of indium-111 and yttrium-88 labeled dendrimer-1B4M-DTPA and its conjugation with anti-Tac monoclonal antibody. Bioconjug. Chem., *10:* 103–111, 1999.
34. Kobayashi, H., Sato, N., Kawamoto, S., Saga, T., Hiraga, A., Haque, T. L., Ishimori, T., Konishi, J., Togashi, K., and Brechbiel, M. W. A novel intravascular macromolecular MR contrast agent with generation-4 polyamidoamine dendrimer core: accelerated renal excretion with co-injection of lysine. Magn. Reson. Med., *46:* 457–464, 2001.
35. Kobayashi, H., Sato, N., Kawamoto, S., Saga, T., Hiraga, A., Ishimori, T., Konishi, J., Togashi, K., and Brechbiel, M. W. 3D MR angiography of intratumoral vasculature using a macromolecular MR contrast agent. Magn. Reson. Med., *46:* 579–585, 2001.
36. Albanell, J., Bellmunt, J., Molina, R., Garcia, M., Caragol, I., Bermejo, B., Ribas, A., Carulla, J., Gallego, O. S., Espanol, T., and Sole Calvo, L. A. Node-negative breast cancers with p53(-)/HER2-neu(-) status may identify women with very good prognosis. Anticancer Res., *16:* 1027–1032, 1996.
37. Rosen, P. P., Lesser, M. L., Arroyo, C. D., Cranor, M., Borgen, P., and Norton, L. Immunohistochemical detection of HER2/neu in patients with axillary lymph node negative breast carcinoma. A study of epidemiologic risk factors, histologic features, and prognosis. Cancer (Phila.), *75:* 1320–1326, 1995.
38. McNeil, C. Herceptin in the adjuvant setting: phase III trials begin. J. Natl. Cancer Inst. (Bethesda), *92:* 683–684, 2000.
39. Baselga, J., Tripathy, D., Mendelsohn, J., Baughman, S., Benz, C. C., Dantis, L., Sklarin, N. T., Seidman, A. D., Hudis, C. A., Moore, J., Rosen, P. P., Twaddell, T., Henderson, I. C., and Norton, L. Phase II study of weekly intravenous trastuzumab (Herceptin) in patients with HER2/neu-overexpressing metastatic breast cancer. Semin. Oncol., *26:* 78–83, 1999.
40. Pegram, M. D., Lipton, A., Hayes, D. F., Weber, B. L., Baselga, J. M., Tripathy, D., Baly, D., Baughman, S. A., Twaddell, T., Glaspy, J. A., and Slamon, D. J. Phase II study of receptor-enhanced chemosensitivity using recombinant humanized anti-p185HER2/neu monoclonal antibody plus cisplatin in patients with HER2/neu-overexpressing metastatic breast cancer refractory to chemotherapy treatment. J. Clin. Oncol., *16:* 2659–2671, 1998.
41. Mandler, R., Wu, C., Sausville, E. A., Roettinger, A. J., Newman, D. J., Ho, D. K., King, C. R., Yang, D., Lippman, M. E., Landolfi, N. F., Dadachova, E., Brechbiel, M. W., and Waldmann, T. A. Immunoconjugates of geldanamycin and anti-HER2 monoclonal antibodies: antiproliferative activity on human breast carcinoma cell lines. J. Natl. Cancer Inst. (Bethesda), *92:* 1573–1581, 2000.
42. Naruki, Y., Carrasquillo, J. A., Reynolds, J. C., Maloney, P. J., Frincke, J. M., Neumann, R. D., and Larson, S. M. Differential cellular catabolism of 111In, 90Y, and ^{125}I radiolabeled T101 anti-CD5 monoclonal antibody. Int. J. Radiat. Appl. Instrum. Part B, *17:* 201–207, 1990.

American Journal of Medical Genetics Part A 143A:3121–3126 (2007)

Visualization of Human Prenatal Development by Magnetic Resonance Imaging (MRI)

Kohei Shiota,[1,2]* Shigehito Yamada,[1] Tomoko Nakatsu-Komatsu,[1] Chigako Uwabe,[1] Katsumi Kose,[3] Yoshimasa Matsuda,[3] Tomoyuki Haishi,[4] Shinobu Mizuta,[5] and Tetsuya Matsuda[5]

[1]Congenital Anomaly Research Center, Kyoto University Graduate School of Medicine, Kyoto, Japan
[2]Department of Anatomy and Developmental Biology, Kyoto University Graduate School of Medicine, Kyoto, Japan
[3]Institute of Applied Physics, University of Tsukuba, Tsukuba, Japan
[4]MRTechnology, Inc., Tsukuba, Japan
[5]Graduate School of Informatics, Kyoto University, Kyoto, Japan

Received 4 July 2007; Accepted 16 July 2007

It is essential to visualize the structures of embryos and their internal organs three-dimensionally to analyze morphogenesis; this used to rely solely on serial histological sectioning and solid reconstruction, which were tedious and time-consuming. We have applied imaging with a magnetic resonance (MR) microscope equipped with a 2.35 T superconducting magnet to visualize human embryos; we were successful in acquiring high-resolution sectional images and in identifying the detailed structures of major organs. The imaging process was facilitated by using a super-parallel MR microscope. A dataset of MR images of more than 1,000 human embryos, now collected, will be important for future biomedical research and for education. © 2007 Wiley-Liss, Inc.

Key words: MR microscope; three-dimensional (3D) visualization; developmental imaging; human embryo

How to cite this article: Shiota K, Yamada S, Nakatsu-Komatsu T, Uwabe C, Kose K, Matsuda Y, Haishi T, Mizuta S, Matsuda T. 2007. Visualization of human prenatal development by magnetic resonance imaging (MRI). Am J Med Genet Part A 143A:3121–3126.

INTRODUCTION

Morphogenesis in the developing embryo takes place in three-dimensions, and the dimension of time is another important factor. Therefore, three-dimensional (3D) and four-dimensional (4D) visualization is essential to understand and analyze dynamic ontogenetic events. Traditionally, major methods of studying developmental anatomy relied on histological sectioning of embryos and solid reconstruction from serial sections to demonstrate the 3D structures of the embryonic body and organs. Well-known examples are the wax models of staged human embryos housed in the Carnegie Embryological Collection [Born, 1883; Heard, 1951, 1953, 1957]. Some of the historical reconstructed models are now preserved in the Human Developmental Anatomy Center in Washington, DC (http://nmhm.washingtondc.museum/collections/hdac/index.htm). Based on those reconstructed models, accurate drawings of human embryos were produced by skillful artists, such as James F. Didusch, who added invaluable information on human prenatal development [O'Rahilly, 1988]. However, such histological sectioning, solid reconstruction, and drawing are time-consuming and require special skills.

During the past 2–3 decades, computer-assisted reconstruction of biological structures has enabled the reconstruction of 3D embryos from serial histological sections with the aid of computer software. It has permitted reconstruction and manipulation of 3D images on the viewing screen. Recently, the Visible Embryo Project was carried out at the US National Museum of Health and Medicine (NMHM), utilizing the human embryo specimens of the Carnegie Col-

Tomoko Nakatsu-Komatsu's present address is Osaka Women's Junior College, Fujiidera, Osaka 583-8558, Japan.

Grant sponsor: Japanese Ministry of Education, Culture, Sports, Science and Technology; Grant number: 19390050; Grant sponsor: Japanese Ministry of Health, Labor and Welfare; Grant number: 17A-6; Grant sponsor: Japan Science and Technology Agency, BIRD Grant.

*Correspondence to: Kohei Shiota, M.D., Congenital Anomaly Research Center, Kyoto University Graduate School of Medicine, Kyoto 606-8501, Japan. E-mail: shiota@anat1.med.kyoto-u.ac.jp

DOI 10.1002/ajmg.a.31994

lection [Cohen, 2002]. Digitized 3D datasets of staged human embryos were completed and are now partly accessible on the web. After the Visible Human Project was discontinued in 2003, the Virtual Human Embryo Project was initiated (http://virtualhumanembryo.lsuhsc.edu/). The project consists of the Digitally Reproduced Embryonic Morphology (DREM) and Human Embryo Imaging and Reconstruction, Library OnLine Media (HEIRLOOM) components, containing high resolution microscopic morphology of human embryos and reconstructed 3D models, respectively. Such image datasets of human embryos are quite valuable, but the process still needs serially sectioned specimens and intensive labor to acquire the desirable precision and refinement of the images.

On the other hand, remarkable progress has been made in nondestructive imaging technologies in clinical medicine, such as computed tomography (CT) and magnetic resonance imaging (MRI). Smith [1999, 2000, 2001] and Smith et al. [1994, 1996, 1999], at Duke University, applied MRI to the visualization of embryos and were successful in obtaining MR images of embryos of both human and laboratory animals. MRI is a nondestructive technique, and efficiently provides 2D sectional images of embryos; 3D images of specimens can then be generated from the sectional data with the aid of computer software.

MRI is such a promising technique for developmental research, but initially, there were some problems and limitations in MRI of small embryos. One was the resolution of MR images, which was not high enough for visualizing fine structures in tiny embryos. To obtain sufficiently high resolution, we introduced a superconducting magnet (2.35 T) to MR microscopy, which significantly improved the quality of the MR images. Another problem was the speed of imaging. It usually takes several hours to image an embryo with MR, which is a serious limiting factor for imaging numerous specimens. This problem was overcome by inventing a super-parallel MR microscope, which enabled imaging of several specimens simultaneously and significantly reduced the time required [Matsuda et al., 2003]. In this article, we describe the "Kyoto Human Embryo Visualization Project," in which over 1,000 cases of staged human embryos are visualized by MR microscopy, and a database of developing human embryo images is established for future biomedical research.

MATERIALS AND METHODS

Embryo Specimens

The human embryo specimens in the Congenital Anomaly Research Center of Kyoto University were used for this study. The majority of the cases were obtained after therapeutic abortions given to healthy women during the first three months of pregnancy. The pregnancies were terminated mainly by dilatation and curettage, which enabled acquisition of undamaged, intact embryos. Further details of the embryo collection have been described in previous reports [Nishimura et al., 1968; Nishimura, 1975; Shiota, 1991; Yamada et al., 2006]. In the present study, approximately 1,400 specimens of externally normal human embryos at Carnegie stage (CS) 13 to CS23 were selected for MR microscopic imaging. The specimens were fixed in 4% formaldehyde or Bouin solution and stored in 4% formaldehyde.

MR Microscopic Imaging

Kose and his coworkers [Matsuda et al., 2003] developed a four-channel MR microscope with four unshielded gradient coil probes. The four-channel array probe was developed for a 2.35 T superconducting magnet. Each gradient coil probe consists of a rigid aluminum square frame [18 cm (W) × 20 cm (H) × 28 cm (D)] and slide planes made of thin brass plates (0.3 mm thick) acting as an RF shield. The RF coil units are exchangeable, and the diameter can be optimized for a given sample size. In the present study, 18 mm diameter four-turn solenoid coils were used for the 100 MHz signal excitation and detection frequency. The pulse sequence was a T_1-weighted 3D gradient echo sequence (TR = 100 ms, TE = 8 ms). Embryo specimens were imaged in test tubes (ID = 13.5 mm) filled with 4% formaldehyde solution. Further details of the MR microscope and its specifications have been described by Matsuda et al. [2003].

RESULTS

Figure 1 shows the 2D cross-sectional images of four fixed human embryos (CS22) selected from simultaneously acquired 3D datasets. The pulse sequence was a T_1-weighted conventional 3D spin-echo sequence (TR = 100 ms, TE = 8ms) and the image matrix size was 128 × 128 × 256. The resolution of these images is 120 μm^3. The images had a similar SNR value and no interference was observed between images acquired simultaneously.

In order to optimize the image contrast, we acquired T_1-weighted images using various repetition times (80–300 ms) and found that the 100 ms repetition gives the best image contrast for staged human embryos (data not shown).

Figure 2 shows that the MR image acquired as above enables identification of the structures in the major organs of human embryos in as much detail as the images of low-magnification histological sections (100× or lower magnification). Thus, it may be possible to identify major structural abnormalities in the embryo by MR microscopy, if there are any.

In Figure 3, 2D sectional images are shown for human embryos at CS18, CS20, and CS22. These

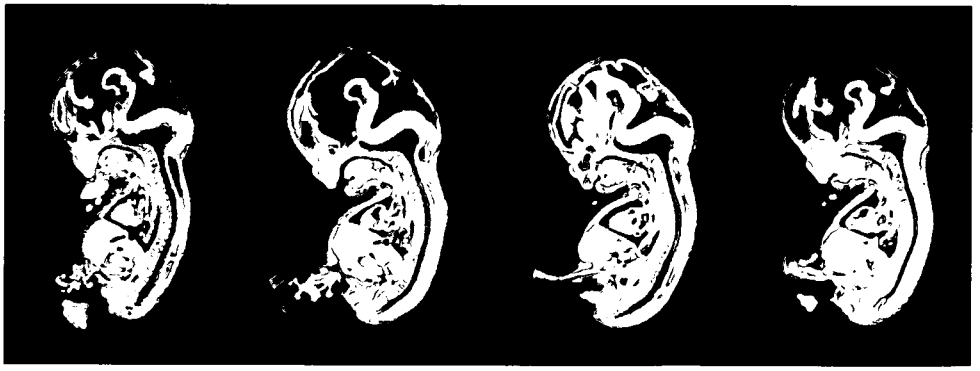

FIG. 1. Sectional images of four human embryo specimens (CS22) acquired simultaneously with the four-channel system of the super-parallel MR microscope. TR/TE = 100 ms/8 ms, spatial resolution = 120 μm^3, image matrix size = 128 × 128 × 256.

sectional MR images again demonstrate major anatomical structures in the embryo, even in those smaller than 20 mm in length.

Using sectional MR images, it is possible to generate the 3D images of each specimen. Figure 4 shows sectional MR images and 3D images of an embryo and its neural tube reconstructed using amira® software (Template Graphics Software, Inc.). The reconstructed images can be rotated on the viewing screen and cut in any desired plane to observe internal structures. Furthermore, 3D images of developing human embryos can be generated and the sequential morphogenetic process can be demonstrated with the aid of a computer graphics technique [Yamada et al., 2006].

DISCUSSION

By using a 2.35 T MR microscope, we acquired sectional 2D images of human embryos; the resolution was equivalent to that of low-magnification histological sections. One of the serious problems in MR imaging is the slow processing speed, and it usually takes several hours to obtain a 3D MR microscopic image dataset at a spatial resolution of a few to several tens of a micrometer [Johnson et al., 1993]. Kose and his coworkers [Matsuda et al., 2003] developed a super-parallel MR microscope, which enabled imaging of 4–8 samples simultaneously, significantly facilitating the speed of image processing. By using the novel super-parallel MR microscope, we could image over 1,000 human embryo specimens in a relatively short period of time (approximately 1 year).

MR imaging is nondestructive and does not need sectioning of embryonic tissues. MR imaging was applied to the embryos of the human and laboratory animals by the pioneering work of Smith [1999, 2000, 2001] and Smith et al. [1994, 1996, 1999]. More recently, Dhenain et al. [2001] applied spin-echo MRI techniques to fixed mouse embryos and identified the structures of the major organs in the embryo. Furthermore, Schneider and his coworkers [Schneider et al., 2003a,b; Schneider and Bhattacharya, 2004] used a

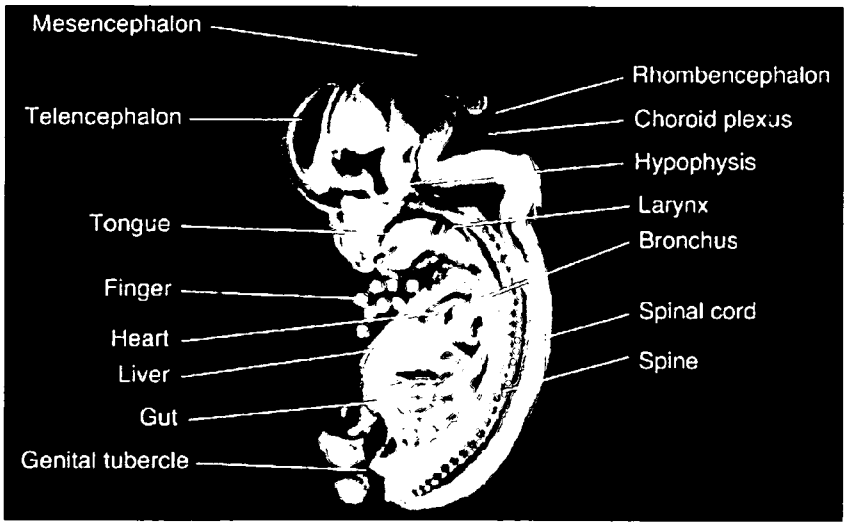

FIG. 2. MR image of a human embryo (CS23) in which structures of the major internal organs are identifiable.

FIG. 3. 2D sectional images of human embryos at CS18, 20, and 22 selected from the datasets of staged human embryos.

T_1-weighted, fast gradient echo MR imaging technique and succeeded in identifying cardiac and other visceral malformations in mutant mouse embryos. By MRI, they visualized normal cardiac structures such as atria and ventricles, atrial and ventricular septa, valves, and great vessels in mouse fetuses as well as various cardiac anomalies, including atrial and ventricular septal defects, outflow tract defects, and malformations of the great vessels in mutant mice. Therefore, it is feasible to apply MR microscopic imaging to fast and efficient screening of embryos in genetic and teratological studies. In addition, if MR microscopy is used for examination of human abortuses, it would help identify internal visceral anomalies quickly, efficiently, and without dissection.

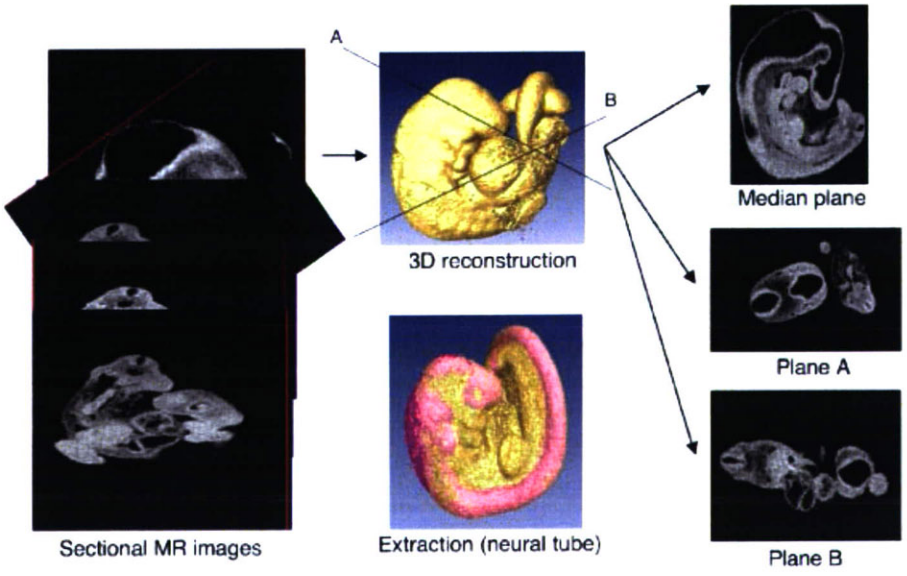

FIG. 4. 3D images of a human embryo and its neural tube (center) reconstructed from sectional MR data (amira® 3.1) and its sectional MR images (left). Sectional images at desired planes can also be generated (right). [Color figure can be viewed in the online issue, which is available at www.interscience.wiley.com.]

Thanks to the recent advancement in MRI technology, the resolution of images has been remarkably improved. In our study, the resolution now approaches 80 μm, and it is possible to identify various embryonic structures, such as the brain (and cerebral cortex), eyes, inner ears, pituitary gland, bronchi, lungs, stomach and intestines, kidneys, gonads, liver and spleen in embryos that are less than 30 mm in length (Fig. 2). We are now visualizing the internal organs of human embryos with external malformations to identify any internal abnormalities that may be present. MRI is nondestructive and does not need sectioning of specimens, which not only saves time and labor, but also allows precious specimens to remain intact. MRI can be complemented with other imaging techniques, such as micro-CT [Shibata and Nagano, 1996], optical projection tomography (OPT) [Sharpe et al., 2002; Sharpe, 2004], and episcopic fluorescence image capture (EFIC) [Weninger et al., 1998; Weninger and Mohun, 2002; Rosenthal et al., 2004] to visualize the detailed 3D and 4D structures in the embryo, and could be used in developmental and teratological research.

Another disadvantage of MRI is its high cost. However, some compact MR apparatuses are available at relatively reasonable cost [Haishi et al., 2001], and the cost of the apparatus might be compensated because MR enables imaging samples continuously, even at night. A super-parallel MR microscope can image four to eight samples simultaneously and contribute to the reduction in cost, as well.

In the "post-sequence" era, it is becoming important to unravel the functions of genes and their interactions in the organism, which cannot be elucidated by conventional molecular biological techniques. To this end, it is necessary to visualize gene expression patterns in the embryo and analyze the 3D and 4D localization of multiple genes in various tissues. The data of gene expression in the embryo obtained by in situ hybridization in single-sections and whole-mount samples can be mapped in 3D images of the embryo, and their dynamic expression patterns can be analyzed. Such databases of dynamic gene expression would help unravel the yet unknown functions, pathways, and interaction of multiple genes in normal and abnormal development. Some 3D databases of developmental gene expression are being furnished for mouse embryos by groups at the University of Edinburgh and MRC [EMAP and EMAGE; Baldock et al., 2003], at the University of Vienna [GeneEMAC; Streicher et al., 2000], and at the Jackson Laboratory [GXD; Smith et al., 2007]. It is hoped that a similar database for human embryos will enable the comparison of developmental gene expression patterns in human and laboratory animals, and provide a clue to identifying new gene functions in the human embryo, as well as gene mutations responsible for human birth defects.

Sequential 3D images of human embryos also have the potential to serve as a reference and an important data resource for human developmental studies similar to the Visible Human Database that contains digitized serial cross-sectional images of normal male and female adult bodies [Ackerman, 1998, 1999] (http://www.nlm.nih.gov/research/visible/visible_human.html). They could serve as models of network-accessible digital image libraries for medical research and education. Actually, various new research projects have emerged from the Visible Human Project, such as the invention of internet-enabled visualization tools and navigation technologies for anatomy education and research; establishing comprehensive atlases of the human body for clinical imaging diagnosis; and virtual reality and surgical simulation for health care education and training [Ackerman et al., 2001]. Similarly, 3D visualization of human embryonic development should be useful in biomedical research and education because such images and movie-illustration of sequential developmental changes would help researchers and students understand the dynamic morphogenetic movements visually that occur in three- and four-dimensions.

ACKNOWLEDGMENTS

The contribution of collaborating obstetricians who provided us with human embryo specimens is gratefully acknowledged. We thank Dr. Mikiko Kobayashi-Miura for generating 3D reconstructed images of embryos. This work was supported by grants of the Japanese Ministry of Education, Culture, Sports, Science and Technology (Grant number 19390050) and the Japanese Ministry of Health, Labor and Welfare (Grant number: 17A-6) and by the BIRD grant of the Japan Science and Technology Agency.

REFERENCES

Ackerman MJ. 1998. The visible human project: A resource for anatomical visualization. Medinfo 9:1030–1032.

Ackerman MJ. 1999. The visible human project: A resource for education. Acad Med 74:667–670.

Ackerman MJ, Yoo T, Jenkins D. 2001. From data to knowledge—The visible human project continues. Medinfo 10:887–890.

Baldock RA, Bard JB, Burger A, Burton N, Christiansen J, Feng G, Hill B, Houghton D, Kaufman M, Rao J, Sharpe J, Ross A, Stevenson P, Venkataraman S, Waterhouse A, Yang Y, Davidson DR. 2003. EMAP and EMAGE: A framework for understanding spatially organized data. Neuroinformatics 1: 309–325.

Born G. 1883. Die Plattenmodelliermethode. Arch Mikr Anat 22:584–599.

Cohen J. 2002. Embryo development at the click of a mouse (News of the week). Science 297:1629.

Dhenain M, Ruffins SW, Jacobs RE. 2001. Three-dimensional digital mouse atlas using high-resolution MRI. Dev Biol 232: 458–470.

Haishi T, Uematsu T, Matsuda Y, Kose K. 2001. Development of a 1.0 T MR microscope using a Nd-Fe-B permanent magnet. Magn Reson Imaging 19:875–880.